Journal of Computational and Applied Mathematics 442 (2024) 115719

Contents lists available at ScienceDirect

Journal of Computational and Applied Mathematics

journal homepage: www.elsevier.com/locate/cam

Robust conservative scheme and nonlinear solver for phase transitions in heterogeneous permafrost

Naren Vohra, Malgorzata Peszynska *

Oregon State University, Department of Mathematics, United States of America

ARTICLE INFO

Keywords:
Nonlinear degenerate parabolic equation
Mixed finite elements
Heat conduction with phase change
Permafrost models
Semismooth Newton's method
Heterogeneous media

ABSTRACT

In this paper we study computational schemes to simulate freezing and thawing in permafrost modeled by a nonlinear heat equation with constitutive properties resembling those in the well known Stefan problem but featuring distinct challenges. The models are discretized with low order conservative discretization and fully implicit time stepping. We explore the challenges due to the nonsmooth nature of the temperature–enthalpy relationship and the domain heterogeneity, with focus on the solver and the use of enthalpy as a primary variable in contrast to the temperature variable used commonly in applications literature. We prove and demonstrate the convergence of our algorithms in realistic physical scenarios.

1. Introduction

In this paper we address the challenges in computational schemes for heat conduction models involving phase transitions in permafrost soils. Our focus is on various forms of heterogeneity and their impact on the solvers. In particular, we demonstrate that the use of enthalpy as primary unknown is by far a more robust choice than the use of temperature variable, even though the latter choice dominates in the applications literature. We provide theoretical explanations and illustrate with numerical experiments. Our work provides a bridge between the rigorous computational mathematics approaches and the permafrost applications literature, with an aim to provide concrete details for computational algorithms in realistic setting, and to annotate their context within rigorous literature results.

In recent years, there has been an increased interest in permafrost modeling due to its role within the global climate studies. Permafrost is formally defined as ground that remains frozen for two or more years [1,2]. The part of permafrost that undergoes annual freezing and thawing is called the active layer; its thickness may range from 0.1 to 1 [m] [3] (Pg. 7). Permafrost features heterogeneity in the form of multiple soil types and ground ice wedges with length scales of 0.01 to 10 [m] [3] (Pg. 8) [4]. A holistic modeling approach involves the study of the thermal, hydrological, and mechanical processes across the scales, and we refer to [5–9] for recent discussion of some modeling aspects, but we do not attempt to give an exhaustive list of references. In this paper we focus only on the thermal aspect of permafrost, and defer the study of the coupled hydrological and mechanical processes to our forthcoming work in [10,11]. We also refer to [12,13] for our first explorations of computational schemes as well as the connection between Stefan problem and permafrost models.

Heat conduction with phase change is modeled with the following nonlinear degenerate parabolic equation, written in the sense of distributions,

$$\partial_t w - \nabla \cdot (k \nabla \theta) = f, \ w \in \alpha(\theta), \tag{1}$$

* Corresponding author.
E-mail address: mpesz@math.oregonstate.edu (M. Peszynska).
URL: http://www.math.oregonstate.edu/~mpesz (M. Peszynska).

https://doi.org/10.1016/j.cam.2023.115719
Received 28 July 2023; Received in revised form 11 November 2023
Available online 5 December 2023

where θ is the temperature, w is the enthalpy which is related to the temperature using the relationship α, $k = k(\theta)$ is the thermal conductivity, and f is an external heat source. For the permafrost models (P), which are our focus here, $\alpha = \alpha^P$ is a nonlinear, piecewise-differentiable, monotone function whose derivative features a singularity at some freezing temperature $\theta = \theta_*$. For the well known Stefan problem, $\alpha = \alpha^{ST}$ is a multivalued graph. We refer to [13] for our work on the connection and the upscaling of Stefan-like models α^{ST} to α^P.

The low regularity of the solutions to (1) for Stefan problem [14] makes finite elements a natural choice for approximation of the temperature θ and enthalpy w variables; see, e.g., [15,16] where proofs of convergence are given. In most works on Stefan and permafrost models θ is approximated using P1 (piecewise-linear) finite elements, and convergence is proven within the so-called Kirchhoff transformation or upon regularization of α^{ST}. The approximation of enthalpy is done separately. For $\theta - w$, we have thus P1-P1 or P1-P0 schemes or P0-P0 schemes, where P0 means piecewise-constant finite elements. For reference, we mention a few works without attempting to provide a comprehensive list. For Stefan problem, P1-P0 schemes with P0 used for enthalpy are in [15,17], but P1-P1 are in [18–20], and P0-P0 finite volume in [21]. For permafrost, P1-P1 is used in [22–25], but P1-P0 or P0-P0 in [26,27]. Furthermore, in some application papers, the schemes apply chain rule in (1) to $w = \alpha^P(\theta)$, with the so called "apparent heat capacity" technique. Such approaches, along with regularizations or model approximations may bear a modeling error significant in permafrost applications relevant especially when coupling (1) to multiphysics scenarios involving thermal or hydrological fluxes.

In this work we focus on permafrost models with the constitutive properties α^P, k^P in $d \geq 1$ dimensions. We use P0-P0 mixed finite element scheme with fully implicit time stepping for approximation of (1) written as

$$\partial_t w + \nabla \cdot q = f,\ w \in \alpha(\theta),\ q = -k\nabla\theta. \tag{2}$$

We introduced the P0-P0 scheme for Stefan problem in this formulation in [12] where we showed it was conservative and compared very well to P1-P0 and P1-P1 approaches. In this paper we focus on P0-P0 schemes and solvers for permafrost applications with heterogeneity. Generally, theoretical techniques such as Kirchhoff transformation or regularizations which are powerful for deriving convergence results do not apply for problems featuring heterogeneity or to coupled multiphysics scenarios. These challenges motivate our focus on solvers and practical scenarios.

Heterogeneity is an important aspect of the processes in porous media including the flow and thermal processes in permafrost, and is associated with the presence of different soil types such as peat, silt, bedrock and gravel which feature different physical properties including the porosity, grain distribution, as well as thermal properties; see, e.g. [23,24,28,29]. To indicate heterogeneity we write $\alpha = \alpha^P(x,\theta)$ and $k = k^P(x,\theta)$; these incorporate distinct soil-type specific properties which may lead to different qualitative behavior, e.g., mild or sharp or even nearly infinite gradients in θ and/or x. A particular heterogeneous medium challenge comes with modeling massive ice or rock wedges embedded in soil; see Fig. 1 for an illustration of the media heterogeneity in permafrost.

Our contributions are as follows. After giving the model details, we begin by (i) analyzing the relationships α^P and $\beta^P = (\alpha^P)^{-1}$ to isolate the challenges specific to permafrost model within the class of nonlinear degenerate parabolic equations. Next, (ii) we discuss the applicability of the known theoretical results for convergence of approximations to (2) to permafrost models. We also discuss numerical methods for (1) in geotechnical engineering and outline their limitations when compared with our P0-P0 scheme. (iii) We define two nonlinear iterative solvers denoted by P0-P0-Θ and P0-P0-W referring to the primary unknowns temperature and enthalpy, respectively. We prove convergence of our nonlinear solvers and demonstrate their robustness when dealing with practical permafrost scenarios and media heterogeneity. We demonstrate the advantages of the enthalpy-based algorithm P0-P0-W over the temperature formulation P0-P0-Θ. Finally, (iv) we provide simulations for physically meaningful heterogeneous scenarios using data from Alaska, USA as well as an example with an ice wedge.

The outline of this paper is as follows. In Section 2 we provide the details of (1) and in Section 3, we define our P0-P0 scheme to discretize (2). We review theory and literature in Section 4. In Section 5 we present our solvers and prove their convergence. In Section 6 we provide numerical examples on the order of convergence as well on the robustness of our solvers, followed by simulations of practical scenarios. We conclude in Section 7 and acknowledgments. Auxiliary results and supplemental data are in the Appendix.

2. Model description

A list of symbols used in this paper is given in Table 1. We provide now the narrative to this notation.

Let $\Omega \subset \mathbb{R}^d,\ d \in \{1,2,3\}$ be a connected open bounded set representing a heterogeneous permafrost domain. We denote by ν the outward normal to $\partial\Omega$.

We assume that Ω is divided into N_r non-overlapping subdomains $\Omega^{(j)}$, where each $\Omega^{(j)}$ is occupied by a particular soil type, or ice, or solid rock. Within each, we denote the variables and data associated with the liquid water, ice, and rock grains by subscripts l, i, and r, respectively. The rock types $j = 1, 2, \ldots, N_r$ have heat capacity and conductivity

$$c_r(x) = c_r^{(j)},\ k_r(x) = k_r^{(j)},\ \forall x \in \Omega^{(j)}. \tag{3}$$

We make the following natural assumptions.

Assumption 2.1. The thermal parameters within each $\Omega^{(j)}$ are constant in x, θ and satisfy

$$0 < c_{min} \leq c_l, c_i, c_r^{(j)} \leq c_{max} < \infty,\ 0 < k_{min} \leq k_l, k_i, k_r^{(j)} \leq k_{max} < \infty,\ 1 \leq j \leq N_r. \tag{4}$$

The latent heat of water $L = \text{const} \geq 0$.

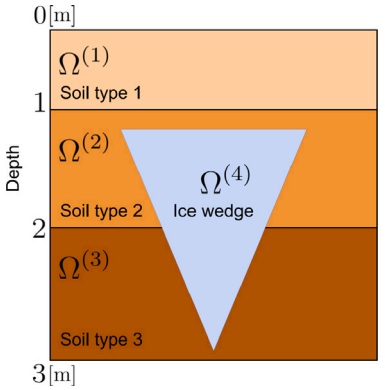

Fig. 1. Illustration of heterogeneity due to multiple soil layers and the presence of ice wedges (motivated by [25,30,31]). In the domains $\Omega^{(j)}, j \in \{1,2,3\}$, the subdomains correspond to different soil types, such as clay, silt, gravel, with the soil type specific temperature enthalpy relationship $\alpha^P(x,\theta)|_{\Omega^{(j)}} = \alpha^{(j)}(\theta)$. In $\Omega^{(4)}$, the thermal properties of ice wedge are $\alpha(x,\theta)|_{\Omega^{(4)}} = \alpha^{ST}(\theta)$ which is multivalued.

Table 1
Variables and parameters in this work.

Subscript/Notation	Description	
$\{l,i,r\}$	Liquid l, ice i (solid) phase, and rock r	
ST, P	Stefan problem (ST) and permafrost models (P)	
SFC	Soil freezing curve	
Variable	**Description/SI Unit**	
θ	Temperature [°C]	
w	Enthalpy/energy per unit volume [J/m^3]	
q	Heat flux [J/m^2 s]	
χ_l	Liquid volume fraction [–]; $\chi_l = \chi_l^P$ or χ_l^{ST}	
Parameter	**Description/SI Unit**	**Typical values**
c	Volumetric heat capacity [J/m^3 °C]	Water 4.19×10^6, Ice 1.9×10^6 [32]
k	Thermal conductivity [J/m s °C]	Water 0.58, Ice 2.3 [32]
L	Latent heat per unit volume [J/m^3]	Water 3.06×10^8 [32]
θ_*	Freezing point depression [°C]	Water 0
η	Porosity [–]	Mineral soil [0.2, 0.4] [24]
Relationship	**Description**	
α	Temperature–enthalpy relationship; $w \in \alpha^{ST}(\theta)$ or $w = \alpha^P(\theta)$	
β	Enthalpy-temperature function $\beta := \alpha^{-1}$; $\theta = \beta^{ST}(w)$ or $\theta = \beta^P(w)$.	

For functional spaces, we consider Lebesgue and Sobolev spaces $M = L^2(\Omega)$ and $X = H_{div}(\Omega)$. The L^2 inner product of scalar valued $f_1, f_2 \in L^2(\Omega)$ or vector valued $f_1, f_2 \in (L^2(\Omega))^d$ is denoted by $(f_1, f_2) = \int_\Omega f_1 f_2$.

2.1. Heat conduction in permafrost soil

The model (1) for permafrost applications reads

$$\partial_t w - \nabla \cdot (k^P(x,\theta)\nabla\theta) = f, \ w = \alpha^P(x,\theta), \tag{5}$$

where the temperature–enthalpy relationship α^P is defined as follows

$$\alpha^P(x,\theta) = \int_{\theta_*}^{\theta} c(x,v)dv + L\eta\chi_l^P(x,\theta), \ c(x,v) = c_f(x) + \chi_l^P(x,v)(c_u(x) - c_f(x)). \tag{6}$$

Here $c_u(x) = c_l\eta(x) + c_r(x)(1-\eta(x))$ and $c_f(x) = c_i\eta(x) + c_r(x)(1-\eta(x))$ are the volumetric heat capacities of "unfrozen" u and "frozen" f soil, respectively [23,24], with η denoting the porosity of the soil, and θ_* denoting the freezing point depression above which water exists only in the liquid phase l. Typically, θ_* is close to 0 [°C] and is used in parametric models for α^P. The water fraction $\chi_l^P = \chi_l^P(x,\theta)$ is called the Soil Freezing Curve and is discussed below.

In turn, the thermal conductivity k^P incorporates the presence of the liquid l, ice i and rock r phases and materials; it is obtained through weighted averaging of the individual thermal conductivities $k_p, p \in \{l,i,r\}$ [6–8,23,33]; see Appendix A.1 for these expressions, and [13] for its proper choice via upscaling.

Table 2
SFC parameters for clay. These parameters have been used to plot Fig. 2.

Model	Parameter values	Adapted from
Adapted L (9a)	$b = 0.271$ [–], $\theta_* = -1.1544$ [°C]	[35] (Figure 9)
Adapted W (9b)	$b = 6.4216$ [°C], $\chi_{res} = 0.36$ [–], $\theta_* = 0$ [°C]	[22] (Table 3)
Adapted M (9c)	$b = 0.16$ [1/°C], $\chi_{res} = 0.20144$ [–] $\theta_* = 0$ [°C]	[6] (Pg. 7)

2.1.1. Soil Freezing Curve (SFC)

The definition (6) involves the water fraction $\chi_l^P(\theta)$; in heterogeneous soil, we have $\chi_l^P = \chi_l^P(x,\theta)$.

Unlike in bulk water (without soil grains), an important feature of permafrost is that $\chi_l^P(\theta)$ is nonzero at a large range of temperatures below some given $\theta_* < 0$; this is due to surface energy effects [34]. In experiments, this measured quantity called the soil freezing curve (SFC) is fit to some algebraic parametric models, and depends on physical and chemical factors such as the specific area of the soil particles, the presence of dissolved solutes and the size of the mineral particles [3,4,35,36].

Generally, $\chi_l^P(\theta)$ is monotone and continuous on $\mathbb{R}$ but not differentiable at $\theta = \theta_*$. However, some of the data reported in literature based on mass fraction measurements [3,35,36] produces discontinuous SFC, with the related numerical difficulties acknowledged in, e.g., [23,33,37]. In fact, the fitted power function SFC expressions used in [35,38,39] are unbounded near $\theta = 0$ [°C], thus they are used only for $\theta \le \theta_* < 0$, or a smooth or regularized SFC [24–26,33] can be considered. Upscaled χ_l^P from our work [13] is also discontinuous but can also be smoothed in practice. In this paper we defer the study of discontinuous SFC to another venue, and focus on other challenges, making the following assumption regarding the SFCs.

Assumption 2.2. (i) For a fixed soil type, the SFC $\chi_l^P(\theta)$ has the general form

$$\chi_l^P(\theta) = \begin{cases} 1; & \theta > \theta_* \\ Y(\theta); & \theta \le \theta_*, \end{cases} \tag{7}$$

where Y is a smooth, monotone nondecreasing, convex, and Lipschitz function which satisfies $0 \le \chi_{res} \le Y(\theta) \le 1,\ \forall \theta \in (-\infty, \theta_*]$; $Y(\theta_*) = 1$, and $\lim_{\theta\to-\infty} Y(\theta) = \chi_{res}$, with Lipschitz constant $L_{\chi_l^P}$ equal that for Y.

(ii) For domains with multiple soil types we have

$$\chi_l^P(x,\theta) = \chi_l^{P^{(j)}}(\theta),\ \forall x \in \Omega^{(j)}, 1 \le j \le N_r, \tag{8}$$

where each $\chi_l^{P^{(j)}}$ satisfies (i).

From Assumption 2.2 χ_l^P is continuous and differentiable except at $\theta = \theta_*$, but globally Lipschitz. In heterogeneous case, χ_l^P is not necessarily continuous in $\Omega \times \mathbb{R}$ thus not globally Lipschitz.

SFC considered in this work. Typically, porous organic soils such as peat and moss have "steep" SFCs, whereas mineral soils such as clay and silt feature a more gradual long tailed behavior. Each satisfies Assumption 2.2, but has different Lipschitz constants. We use one of three SFCs adapted from [22,35,37] denoted with superscripts L, W and M corresponding to the original author's names. Their expressions and the Lipschitz constants for χ_l^P are given

$$Y^L(\theta) = |\theta_*|^b |\theta|^{-b},\quad L_{Y^L} = b|\theta_*|^{-1}, \tag{9a}$$

$$Y^W(\theta) = \chi_{res} + (1-\chi_{res}) b^4 (b - \theta + \theta_*)^{-4},\quad L_{Y^W} = 4(1-\chi_{res}) b^{-1}, \tag{9b}$$

$$Y^M(\theta) = \chi_{res} + (1-\chi_{res}) e^{b(\theta-\theta_*)},\quad L_{Y^M} = (1-\chi_{res}) b. \tag{9c}$$

See illustrations in Fig. 2, with typical data in Table 2.

2.1.2. Properties of temperature–enthalpy function α^P

We prove now some properties of α^P and its inverse $\beta^P = (\alpha^P)^{-1}$.

Lemma 2.1. *Let Assumption 2.1 and 2.2 hold and α^P be given by (6). Then α^P is continuous, piecewise-smooth, globally Lipschitz, and strictly monotone. Further, $|(\alpha^P)'|$ whenever defined is bounded above and below by positive constants. Moreover, $\beta^P = (\alpha^P)^{-1}$ is well-defined and is also continuous, piecewise-smooth, globally Lipschitz, and strictly monotone with derivative $|(\beta^P)'|$ bounded above and below by positive constants, except at $w = w_* = \alpha^P(\theta_*)$, where β^P is non-differentiable.*

Proof. We set $(A^P)'(\theta) = c_u \chi_l^P(\theta) + c_f(1 - \chi_l^P(\theta)) + L\eta(\chi_l^P)'(\theta)$ and calculate from (6)

$$(\alpha^P)'(\theta) = \begin{cases} c_u; & \theta > \theta_* \\ (A^P)'(\theta); & \theta < \theta_*. \end{cases} \tag{10}$$

Now we see $(\alpha^P)'$ is discontinuous at $\theta = \theta_*$. Further, from Assumptions 2.1 and 2.2, A^P is smooth and each term in the definition of $(A^P)'$ is positive, and since $\chi_l^P \in [0,1]$, we can conclude that $(A^P)' \ge \min\{c_u, c_f\} \ge c_{min}$. Also, at $\theta = \theta_*$ we have

$$\lim_{\theta\to\theta_*^+} (\alpha^P)'(\theta) = c_u,\ \lim_{\theta\to\theta_*^-} (\alpha^P)'(\theta) = c_u + L\eta \lim_{\theta\to\theta_*^-} (\chi_l^P)'(\theta),$$

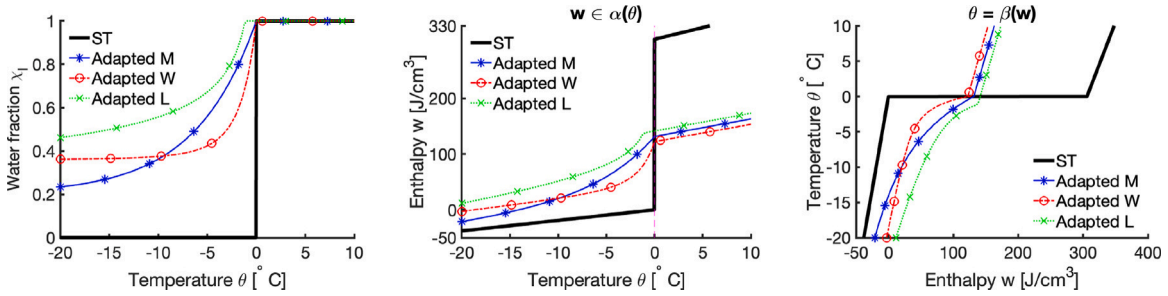

Fig. 2. Illustration of the water fraction χ_l (left) and temperature–enthalpy relationships α (middle) and β (right) for the permafrost model compared to Stefan problem. Note that χ_l^{ST} and α^{ST} are multivalued at $\theta = \theta_*$, whereas χ_l^P and α^P are functions with a long tailed behavior as $\theta \to -\infty$. Here we use the SFC and thermal parameters for clay and water as listed in Tables 2 and 5.

and thus

$$[(\alpha^P)']_{\theta_*} = -L\eta \lim_{\theta \to \theta_*^-} (\chi_l^P)'(\theta). \tag{11}$$

Now we see that the upper bound and Lipschitz constant is

$$|(\alpha^P)'(\theta)| \le (c_{max} + L\eta L_{\chi_l^P}) = L_{\alpha^P} \tag{12}$$

which can be found in practice for each SFC from (9).

We may further prove that

$$\alpha^P(\theta_2) - \alpha^P(\theta_1) \ge c_{min}(\theta_2 - \theta_1),\ \forall \theta_1, \theta_2 \in \mathbb{R}, \theta_1 \le \theta_2. \tag{13}$$

Indeed, for $\theta_1 < \theta_2$, since χ_l^P is monotone, we have from (6)

$$\alpha^P(\theta_2) - \alpha^P(\theta_1) \ge \int_{\theta_1}^{\theta_2} \left(c_u \chi_l^P(v) + c_f(1 - \chi_l^P(v))\right) dv \ge \min\{c_u, c_f\}(\theta_2 - \theta_1) \ge c_{min}(\theta_2 - \theta_1).$$

This proves (13) and consequently that α^P is strictly increasing monotone.

Since α^P is continuous and strictly monotone, β^P is well-defined and continuous. Further,

$$(\beta^P)'(w) = \frac{1}{(\alpha^P)'(\beta^P(w))} = \begin{cases} \frac{1}{c_u}; & w > w_* \\ \frac{1}{(A^P)'(\beta^P(w))}, & w < w_*, \end{cases} \quad w_* = \alpha^P(\theta_*), \tag{14}$$

thus β^P is piecewise-smooth. Moreover, from (12) and (13) we have $\forall w_1, w_2 \in \mathbb{R}$

$$\frac{1}{\left(c_{max} + L\eta L_{\chi_l^P}\right)} |w_2 - w_1| \le |\beta^P(w_2) - \beta^P(w_1)| \le \frac{1}{c_{min}} |w_2 - w_1|. \tag{15}$$

Hence β^P is globally Lipschitz, strictly monotone, and differentiable except at w_*. □

From Lemma 2.1, it follows immediately that α^P and β^P are semismooth on $\mathbb{R}$ [40] (Pg. 35, Prop. 2.26). In fact, since α^P and β^P are piecewise-smooth, they are order 1-semismooth. We also make the following observation when comparing the behavior of α^P and β^P. From (15), it follows that $(\beta^P)' \le c_{min}^{-1}$ even when χ_l^P features steep gradients. This is in contrast with a large slope of α^P near $\theta \approx \theta_*$ and its jump given in (11). These features support the improved robustness of our P0-P0 solver in the enthalpy formulation over the temperature formulation discussed in Section 5.

2.2. Heat conduction in ice wedges

In heterogeneous permafrost, it is common to encounter subdomains filled with ice wedges of considerable size, where porosity $\eta = 1$, i.e., there are no soil grains. In such subdomains, the model (1) takes the form of the well-known Stefan problem [12,14,41,42] where $\alpha = \alpha^{ST}$ and $k = k^{ST}$. For completeness we provide its definition now, in a form consistent with (6) in which we set $\eta = 1$, and use $\chi_l^{ST}(\theta) = \mathscr{H}(\theta - \theta_*)$, where $\mathscr{H}$ is the Heaviside graph with $\mathscr{H}(v) = 0,\ \forall v < 0,\ \mathscr{H}(v) = 1,\ \forall v > 0$, and $\mathscr{H}(0) = [0, 1]$.

We obtain multivalued $\alpha = \alpha^{ST}$ given by

$$\alpha^{ST}(\theta) = \int_{\theta_*}^{\theta} c(v)dv + L\chi_l^{ST}(\theta),\ c(\theta) = \begin{cases} c_l; & \theta > \theta_* \\ c_i; & \theta < \theta_*, \end{cases} \tag{16}$$

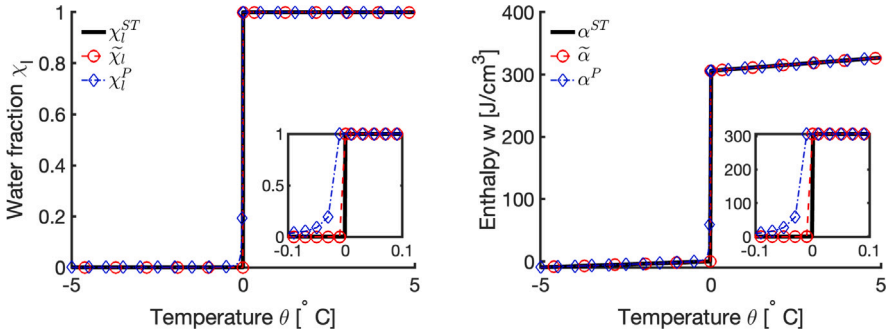

Fig. 3. Illustration of approximations to χ_l^{ST} (left). Plotted are χ_l^{ST} as well as its piecewise-linear $\widetilde{\chi_l}$ given by in (19) with $\epsilon = 0.01$ [°C], and the adapted L permafrost SFC function χ_l^P with $b = 1.5$, $\theta_* = -0.01$ [°C] in (9a). The corresponding α^{ST} and its approximations by (16) are shown on right.

with its inverse function $\beta^{ST} = (\alpha^{ST})^{-1}$ given by

$$\beta^{ST}(w) = \begin{cases} \frac{w-L}{c_l} + \theta_*; & w > L \\ \theta_*; & w \in [0, L] \\ \frac{w}{c_i} + \theta_*; & w < 0. \end{cases} \tag{17}$$

In turn, the thermal conductivity $k = k^{ST}$ is given by

$$k^{ST}(\theta) = \begin{cases} k_l; & \theta > \theta_* \\ k_i; & \theta < \theta_*, \end{cases} \quad k^{ST}(\theta_*) = \frac{k_i + k_l}{2}. \tag{18}$$

Now we discuss the properties of α^{ST} and β^{ST}. In comparison with those of α^P, β^P given in Lemma 2.1, we see that α^{ST} is a monotone multi-valued graph with singularity at $\theta = \theta_*$. In turn, the function β^{ST} is globally Lipschitz, piecewise-linear, and thus semismooth. A plot of α^{ST} and β^{ST} is included in comparison with α^P and β^P in Fig. 2.

2.2.1. Approximating χ_l^{ST} and α^{ST}

As mentioned in Introduction, theoretical results and practical computational models of Stefan problem frequently approximate the multivalued graph χ_l^{ST} as well as the resulting α^{ST} with functions of finite slopes. In heterogeneous models involving permafrost with ice wedges, it is possible to set up domain decomposition and not regularize. However, in this paper, we consider two approximations $\widetilde{\chi_l^{ST}}$ to χ_l^{ST}. One is (i) a piecewise-linear approximation $\widetilde{\chi_l} \approx \chi_l^{ST}$

$$\widetilde{\chi_l}(\theta) = \begin{cases} 0; & \theta < \theta_* - \epsilon \\ \frac{(\theta - \theta_* + \epsilon)}{\epsilon}; & \theta \in [\theta_* - \epsilon, \theta_*] \quad \epsilon > 0. \\ 1; & \theta > \theta_*, \end{cases} \tag{19}$$

We also consider (ii) a sufficiently steep SFC, e.g., the adapted L SFC (9a) with a high b and a small $|\theta_*|$. The corresponding approximation $\widetilde{\alpha^{ST}} \approx \alpha^{ST}$ are calculated with (16). An illustration of $\widetilde{\chi_l^{ST}}$ and $\widetilde{\alpha^{ST}}$ is shown in Fig. 3.

3. Approximation scheme

To approximate the solutions to (2) we use the lowest order mixed finite elements: we approximate the temperature and enthalpy with P0 elements enforcing $w = \alpha^P(\theta)$ pointwise for each degree of freedom and flux q with $\mathrm{RT}_{[0]}$ element. We provide details below, assuming for simplicity homogeneous Dirichlet boundary conditions $\theta|_{\partial\Omega} = 0$. We also assume some given initial data $w_0 \in M$.

For simplicity of notation, we consider $\Omega \subset \mathbb{R}^2$, and assume Ω can be well covered by a rectangular grid $\mathscr{T}^h$ with N_ω elements $\omega_{i,j}$ so that $\overline{\Omega} = \bigcup_{i,j} \omega_{i,j}$, with each $\omega_{i,j}$ having cell widths $h_{x,i}, h_{y,j}$ in the x and y direction, respectively. We also assume that the grid edges align with any material interfaces. We further denote $h_{min} = \min_{i,j}\{h_{x,i}, h_{y,j}\}$ and $h_{max} = \max_{i,j}\{h_{x,i}, h_{y,j}\}$. Each cell $\omega_{i,j}$ has edges $\gamma_{i-\frac{1}{2},j}, \gamma_{i,j+\frac{1}{2}}, \gamma_{i+\frac{1}{2},j}$ and $\gamma_{i,j-\frac{1}{2}}$ when listed clockwise from its left edge.

On $\mathscr{T}^h$ we consider the space of piecewise-constant functions $M_h \subset M$ (P0) and the lowest order Raviart–Thomas space $X_h = RT_{[0]} \subset X$. We also use the generic subscript h in $(\cdot,\cdot)_h$ to denote the use of the trapezoidal-midpoint (TM) quadrature for numerical integration [43,44]. In the end, the discretization is implemented as a cell-centered finite difference/finite volume scheme.

We consider a time grid $t_n = t_{n-1} + \tau_n,\ 1 \le n \le N,\ t_0 = 0$, where τ_n is the time step. Our fully discrete implicit P0-P0 mixed element scheme at each $1 \le n \le N$, given $w_h^{n-1} \in M_h$ seeks $(\theta_h^n, q_h^n) \in M_h \times X_h$ such that

$$(w_h^n, \eta_h) + \tau_n(\nabla \cdot q_h^n, \eta_h) = (w_h^{n-1} + \tau_n f^n, \eta_h),\ \forall \eta_h \in M_h,\ w_h^n \in \alpha(\theta_h^n), \tag{20a}$$

$$(\widetilde{k}^{-1} q_h^n, \psi_h)_h - (\theta_h^n, \nabla \cdot \psi_h) = 0,\ \forall \psi_h \in X_h, \tag{20b}$$

where $\widetilde{k} \in M_h$ is a suitable approximation to $k(\theta_h^n)$ based on time or iterative lagging to be discussed in Section 5, and has similar properties to k so that $\widetilde{k}^{-1}$ is well-defined. The use of the $(\cdot,\cdot)_h$ quadrature allows us to eliminate q_h and implement (20) as a cell-centered finite difference (CCFD) scheme for θ_h^n, w_h^n.

Next we rewrite (20) in the matrix–vector as a nonlinear algebraic system; here we follow notation from [12]. The basis functions of M_h are simply the indicator functions $\mathbf{1}_{\omega_{i,j}}$. For $\theta_h, w_h \in M_h$, we denote by $\Theta_{i,j} = \theta_h|_{\omega_{i,j}}$ and $W_{i,j} = w_h|_{\omega_{i,j}}$. The vector-valued functions of X_h are tensor products of piecewise-linear functions in one direction and piecewise-constants in the other direction. For any $q_h = (q_{h1}, q_{h2}) \in X_h$, q_{h1} and q_{h2} are defined by their values on the edges $\gamma_{i\pm\frac{1}{2},j}$ and $\gamma_{i,j\pm\frac{1}{2}}$, respectively, and we denote $Q_{i\pm\frac{1}{2},j} = q_{h1}|_{\gamma_{i\pm\frac{1}{2},j}}$ and $Q_{i,j\pm\frac{1}{2}} = q_{h2}|_{\gamma_{i,j\pm\frac{1}{2}}}$. We denote the basis functions for X_h by $\psi_{i+\frac{1}{2},j}$ for first component and by $\psi_{i,j+\frac{1}{2}}$ for the second component. Finally, the vector F collects the entries $F_{i,j} = (f, \mathbf{1}_{\omega_{i,j}})$. Let Θ, W, and Q denote the degrees of freedom of θ_h, w_h, and q_h, respectively, in their respective basis.

Let $\mathscr{M}$ be the mass matrix defined by $(w_h, \theta_h) = \Theta^T \mathscr{M} W,\ \forall \theta_h, w_h \in M_h$; for a uniform square spatial grid $\mathscr{M} = h^2 I_{N_\omega \times N_\omega}$. We denote by $\mathscr{B}$ the matrix defined by $(\nabla \cdot q_h, \theta_h) = -\Theta^T \mathscr{B} Q,\ \forall \theta_h \in M_h, q_h \in X_h$, and by $\widetilde{\mathscr{K}}$ the matrix defined by $(\widetilde{k}^{-1} q_h, \phi_h)_h = \Phi^T \widetilde{\mathscr{K}} Q,\ \forall q_h, \phi_h \in X_h$, where Φ denotes the degrees of freedom of ϕ_h. With these, (20) can be written as

$$\mathscr{M} W^n - \tau_n \mathscr{B} Q^n = \tau_n F^n + \mathscr{M} W^{n-1},\ W^n \in \alpha(\Theta^n), \tag{21a}$$

$$\mathscr{B}^T \Theta^n + \widetilde{\mathscr{K}} Q^n = 0, \tag{21b}$$

where we use the superscript to denote the time step. Since the matrix $\widetilde{\mathscr{K}}$ is diagonal and invertible (see Appendix A.2 below), we can easily eliminate Q^n to get

$$\mathscr{M} W^n + \tau_n \mathscr{A} \Theta^n = \tau_n F^n + \mathscr{M} W^{n-1}, \tag{22}$$

where $\mathscr{A} := \mathscr{B} \widetilde{\mathscr{K}}^{-1} \mathscr{B}^T$, with details in Appendix A.2. The model is closed with a component-wise relationship between W^n and Θ^n, a counterpart of $w = \alpha^P(\theta)$ or $\theta = \beta^P(w)$. In the former case, we have the temperature formulation with primary unknown Θ^n. In the latter, we have the enthalpy formulation with W^n as primary unknown.

The problem (22) is nonlinear, and must be solved by iteration which we discuss in Section 5.

4. Literature review on convergence rates and numerical models

In this section we identify and briefly review the literature context relevant for our scheme (22) for the permafrost model (5), as a specific case of (1). First in Section 4.1 we discuss known results on mixed finite element approximation to degenerate parabolic problems of a structure as in (1). In Section 4.2 we recall the schemes used specifically for (5) in the applications literature and discuss their features in contrast to our scheme (22).

4.1. Orders of convergence derived in literature

We are not aware of any rigorous work in computational mathematics literature devoted to the specific challenges of permafrost modeled by (5). If framed as a generic doubly nonlinear degenerate parabolic problems with structure (1), the analysis of mixed finite element schemes as well as their CCFD formulation is well known, and the order of convergence depends on the character of nonlinearity in (1).

For the simplest linear case when $\alpha(\theta) = c\theta,\ c = const$ and $k = k(x)$ in (1), under Neumann boundary conditions and strong regularity assumptions on θ and q, [45] (Thm. 5.1) derives the estimates

$$\|\theta_h - \theta\|_{\infty,2} + \max_n \left(k^{-1}(q_h^n - q^n), q_h^n - q^n\right)_h^{\frac{1}{2}} = O(h^2 + \tau). \tag{23}$$

For nonlinear $\alpha(\theta)$ and $k = k(x)$ motivated by applications in reservoir engineering, the analysis in [46] is based on Kirchhoff framework. The Kirchhoff transform is defined as $K : \mathbb{R} \to \mathbb{R},\ K(\theta) = \int_{\theta_*}^{\theta} k(v)dv$. One defines the Kirchhoff temperature $u = K(\theta)$, and change variables in (1) as

$$\partial_t w - \Delta u = 0. \tag{24}$$

Further using $\theta = \beta(w)$ we have

$$u = P(w),\ P := K \circ \beta. \tag{25}$$

For the degenerate case, when $(P)'(w)$ vanishes for some values of $w \in \mathbb{R}$ (as in Stefan problem), [46] (Theorem 3) provides optimal estimates of the form

$$\sum_{m=1}^{n} \tau_m \left(w_h^m - w^m, P(w_h^m) - P(w^m) \right) + \left\| \sum_{m=1}^{n} \Psi_h^m \tau_m - \Pi_h^1 \int_0^{t_n} \Psi \right\|_2 = O(h+\tau), \tag{26}$$

where $\Psi = -\nabla u$, and $\Pi_h^1 : L^2(\Omega)^d \to X_h$ is the L^2 projection operator. For the nondegenerate case, i.e., when $(P)' \neq 0$ (such as for permafrost models), under strong assumptions of smoothness of P and $(P)'$, [46] (Theorem 5) proves the estimate

$$\|w_h - w\|_{\infty,2} + \|\Psi - \Psi_h\|_{2,2} = O(h+\tau). \tag{27}$$

Further, [46] (Theorem 7) extends (27) to superconvergent orders on rectangular grids, i.e.,

$$\|w_h - \Pi_h^0 w\|_{\infty,2} + \|\Psi - \Pi_h^1 \Psi_h\|_{2,2} = O\left(h^2 + \tau\right), \tag{28}$$

where $\Pi_h^0 : L^2(\Omega) \to M_h$ is the L^2 projection operator.

In turn, [47] (Theorem 2) focuses on the case of Richards equation, where the authors prove first order convergence assuming that P^{-1} is continuously differentiable and Lipschitz

$$\left\| \sum_{m=1}^{N} \int_{t_{m-1}}^{t_m} (u_h^m - u^m) \right\|_2 + \left\| \sum_{m=1}^{N} \int_{t_{m-1}}^{t_m} (\Psi_h^m - \Psi) \right\|_2 = O(h+\tau). \tag{29}$$

Also for Richards equation, optimal orders are given in [48] (Thm. 5.2), who consider an expanded mixed finite element scheme and prove

$$\|\theta_h - \theta\|_{\infty,2} + \|\tilde{q}_h - \tilde{q}\|_{2,2} = O(h+\tau), \tag{30}$$

where $\tilde{q} = -\nabla\theta$.

Remark 4.1. The orders of convergence given by (27)–(29) require that α or P for (1) are smooth and are derived by employing a mean value argument which requires $|(P)''|$ to be well-defined and bounded. This assumption does not hold for permafrost model (5) since the corresponding $P = K \circ \beta^P$ is only piecewise-smooth. Indeed, from Lemma 2.1

$$(P)'(w) = k^P\left(\beta^P(w)\right)(\beta^P)'(w), \ w \neq w_*, \tag{31}$$

and $(P)'$ is discontinuous at $w = w_*$, i.e, $(P)''$ features the Dirac delta $\delta(w - w_*)$ and is not a well-defined function. Thus, the estimates (27)–(29) do not formally apply to (5). Furthermore, any arguments based on Kirchhoff transformation do not apply to heterogeneous problems.

In spite of that theoretical results do not apply to the permafrost model, we show that our P0-P0 scheme leads to linear orders of convergence for θ, w, and q robustly for realistic permafrost scenarios, with quadratic superconvergence similar to that (28) for temperatures all strictly above, or all below θ_*, in homogeneous media. Thus, the scheme (22) for (5) appears well grounded in theory even if the rigorous results from the literature do not apply directly.

4.2. Schemes in the applications literature

The majority of numerical models in the permafrost applications literature are based on P1 finite element or nodal finite difference approaches, and exploit the "apparent heat capacity" concept, essentially an application of the chain rule; see [6,23–25,28,33,49,50]. This involves rewriting (5) as

$$c_{app}(\theta)\partial_t\theta - \nabla\cdot(k^P\nabla\theta) = f, \ c_{app}(\theta) := c(\theta) + \eta L(\chi_l^P)'(\theta), \tag{32}$$

where $c_{app}(\theta) = (\alpha^P)'(\theta)$ is the "apparent heat capacity". Such an approach allows an evaluation of c_{app} by time-lagging and appears natural. However, (i) the non-smooth behavior of α^P at $\theta = \theta_*$ with the jump of the derivative given by (11) and (ii) steep gradient of c_{app} near θ_* lead to difficulties. These features pose a challenge for P1 schemes when mass matrices involving c_{app} are computed unless a fine mesh and appropriate numerical quadrature is used, since the contribution of the latent heat term at phase change may not be captured properly [51–53]. These difficulties are not present for our P0-P0 scheme since we handle $w = \alpha(\theta)$ in (22) directly without chain rule

The difficulty presented by (i) is avoided by some by considering appropriate smooth approximations of χ_l^P [24,25]. For (ii), if the enthalpy $w_h^n = \alpha^P(\theta_h^n)$ is interpolated using P1 elements, certain "spatial" [49,54] or "temporal" [55] averaging methods are employed, and improve the performance of the scheme over the direct use of (32). Recently, techniques similar to the temporal averaging were employed in [24,25] to approximate $(\chi_l^P)'(\theta)$ in (32), while in [23], χ_l^P is used as the integrating variable in evaluating mass matrices. In turn, in [26,27] the enthalpy formulation is used, but $(\alpha^P)'$ is approximated with a finite difference approximation. The resulting nonlinear system of equations is usually solved by the Newton's or Picard's method [23,25,26,28].

While some of the above approximations seem natural to implement, the use of chain rule involving c_{app} is not conservative since $\alpha^n - \alpha^{n-1} \neq c_{app}(\theta^n - \theta^{n-1})$. Further, the use of regularized SFCs or c_{app} approximations lead to modeling errors.

Our P0-P0 algorithms do not suffer from these issues since the semismooth framework for Newton's method allows us to consider non-smooth SFCs (see Assumption 2.2) without any need for regularization or chain rule application.

5. Computational algorithm and solver

In this section we provide details of solvers for our P0-P0 algorithm (22) in both the temperature and enthalpy variants, with a solver based on Newton's iteration. First we provide implementation details and next we analyze the nonlinear solver, and show that it is robust and efficient.

The standard Kantorovich result for convergence of Newton iteration requires the nonlinearity to be smooth with Lipschitz continuous derivative [56]. However in the permafrost models and scheme (22), we only have piecewise-smoothness for the nonlinearities α and β. Thus we work in the semismooth framework [40,57] which establishes super-linear or even quadratic convergence under some assumptions. In practice, we obtain quadratic convergence for an appropriate initial guess.

Second, nonlinear solvers based on the Newton's method are well known to be quadratically convergent but require a good enough initial guess for convergence. For transient problems, this means the Newton solver may require small time steps for robust convergence. These are frequently the reasons why researchers consider other schemes, e.g., the L-scheme is considered in [58] for the Richards' equation, while recent work on Anderson acceleration improves over Newton's and Picard's methods for stationary problems in [59]. However, we find that accurate simulation of the dynamics of the free boundary in permafrost (or Stefan problem) requires moderate size time steps anyway; with these, our solver is robust.

5.1. Implementation details

First we complete (22) by the relationship between W and Θ, the counterpart of $w = \alpha^P(\theta)$. Both are solved by iteration until the residuals achieve an absolute tolerance of 10^{-12} or a relative tolerance of 10^{-6} (with respect to the first iteration). Further, we use adaptive time stepping: at every $t = t^n$, starting with an initial fixed $\tau_n = \tau$, if convergence of our algorithm is not achieved within $m_{max} = 30$ iterations, we repeat the step with reduced time step $\tau_n = \frac{\tau}{2}$. If not successful, we continue the reduction further.

Temperature formulation: at each time step t^n we seek Θ^n such that

$$\mathscr{M}\alpha^P(\Theta^n) + \tau_n \mathscr{A}\Theta^n = \tau_n F^n + \mathscr{M}W^{n-1}, \tag{33}$$

We solve the problem by iteration, with an initial guess $\Theta^{n,(0)} = \Theta^{n-1}$.

In each iteration $m = 1, 2, \ldots$, given $\Theta^{n,(m-1)}$, we find $\Theta^{n,(m)}$ as

$$\text{(P0-P0-}\Theta\text{)} \begin{cases} R(\Theta^{n,(m-1)}) = \mathscr{M}\alpha^P(\Theta^{n,(m-1)}) + \tau_n \mathscr{A}\Theta^{n,(m-1)} - \mathscr{M}W^{n-1} - \tau_n F^n, & \text{(a)} \\ (\mathscr{M}\mathscr{J}_\alpha^{n,(m-1)} + \tau_n \mathscr{A})\delta\Theta^{n,(m)} = -R(\Theta^{n,(m-1)}), & \text{(b)} \\ \Theta^{n,(m)} = \Theta^{n,(m-1)} + \delta\Theta^{n,(m)}, & \text{(c)} \end{cases} \tag{34}$$

where $\mathscr{J}_\alpha^{n,(m-1)} \in \partial\alpha^P(\Theta^{n,(m-1)})$ is a diagonal matrix. We note that (34)(b) involves solving a linear system. Also, $\partial\alpha^P$ is the Clarke's generalized Jacobian defined as the convex hull $\partial\alpha^P = \text{co}(\partial_B\alpha^P)$, with the B-subdifferential

$$\partial_B\alpha^P(\theta) = \{J_\alpha \in \mathbb{R} \mid \exists\{\theta_k\}_k \in D_\alpha, \theta_k \to \theta, (\alpha^P)'(\theta_k) \to J_\alpha\}, \tag{35}$$

where $D_\alpha \subset \mathbb{R}$ is the set where α^P admits a Fréchet derivative.

Now we need to state how we make the selection out of $\partial\alpha^P$ in our implementation. We use $\partial\alpha^P(\theta) = (\alpha^P)'(\theta), \forall\theta \neq \theta_*$. Also, we set $\partial\alpha^P(\theta_*) = c_u$.

Enthalpy formulation: we seek W^n such that

$$\mathscr{M}W^n + \tau_n \mathscr{A}\beta(W^n) = \tau_n F^n + \mathscr{M}W^{n-1}, \tag{36}$$

with $\beta = \beta^P$ or β^{ST}. We start with an initial guess $W^{n,(0)} = W^{n-1}$. Next, we consider the enthalpy formulation (36): in each iteration m, given $W^{n,(m-1)}$, we find $W^{n,(m)}$ as follows

$$\text{(P0-P0-}W\text{)} \begin{cases} R(W^{n,(m-1)}) = \mathscr{M}W^{n,(m-1)} + \tau_n \mathscr{A}\beta(W^{n,(m-1)}) - \mathscr{M}W^{n-1} - \tau_n F^n, & \text{(a)} \\ (\mathscr{M} + \tau_n \mathscr{A}\mathscr{J}_\beta^{n,(m-1)})\delta W^{n,(m)} = -R(W^{n,(m-1)}), & \text{(b)} \\ W^{n,(m)} = W^{n,(m-1)} + \delta W^{n,(m)}, & \text{(c)} \end{cases} \tag{37}$$

where $\mathscr{J}_\beta^{n,(m-1)} \in \partial\beta(W^{n,(m-1)})$ is Clarke's generalized Jacobian, a diagonal matrix. In our implementation, we set $\partial\beta^P(w_*) = {c_u}^{-1}$ for permafrost models and $\partial\beta^{ST}(0) = 0$, $\partial\beta^{ST}(L) = {c_l}^{-1}$ for the Stefan problem.

Finally, the algebraic expression for β^P in (37)(a) is not easy to find explicitly, and the use of look-up tables to invert some piecewise-linear $\widetilde{\alpha^P} \approx \alpha^P$ leads to a modeling error and discrepancy between the results obtained with P0-P0-Θ and P0-P0-W.

For our numerical experiments, we employ a local nonlinear solver to invert $\beta^P(W^{n,(m-1)})$ componentwise in (37)(a), i.e., we need to solve $\alpha^P(\Theta_{ij}^{n,(m-1)}) - W_{ij}^{n,(m-1)} = 0$ in every cell ω_{ij}. For this purpose, we choose Ridder's method [60] (Pg. 452) which is

known to be very robust; we apply the same relative and absolute tolerances as those listed above. In our experiments, Ridder's method converges within a maximum of 25 iterations and an average of 3 iterations.

5.2. Convergence of solvers P0-P0-Θ and P0-P0-W

Now we demonstrate theoretical results for our algorithms. For these, we time-lag the conductivity values $\widetilde{k} = k(\theta_h^{n-1})$ in (20b).

Lemma 5.1. *At each time step n, the sequence $\{\Theta^{n,(m)}\}_m$ generated by (34) converges quadratically to the solution Θ^n of (33) for an appropriate initial guess.*

Proof. From Lemma 2.1 $\mathscr{J}_\alpha^{n,(m-1)}$ has positive entries. Moreover, since $\mathscr{M}$ is the diagonal matrix of cell volumes, the product $\mathscr{M}\mathscr{J}_\alpha^{n,(m-1)}$ is diagonal and the eigenvalues $\lambda\left(\mathscr{M}\mathscr{J}_\alpha^{n,(m-1)}\right) \geq h_{min}^2 c_{min}$. Since $\mathscr{A}$ is symmetric positive semidefinite, the Jacobian $\mathbb{J}_\alpha^{n,(m-1)} = \mathscr{M}\mathscr{J}_\alpha^{n,(m-1)} + \tau_n\mathscr{A}$ in (34)(b) is symmetric positive definite and thus invertible.

Now, since $\lambda\left(\mathbb{J}_\alpha^{n,(m-1)}\right) \geq \min\left\{\lambda\left(\mathscr{M}\mathscr{J}_\alpha^{n,(m-1)}\right)\right\}$, we have

$$\left\|\left(\mathbb{J}_\alpha^{n,(m-1)}\right)^{-1}\right\|_2 \leq \frac{1}{h_{min}^2 c_{min}}. \tag{38}$$

Finally, since α is order-1 semismooth, we see that the sequence $\{\Theta^{n,(m)}\}_m$ generated by the semismooth Newton's method will converge quadratically for an appropriate initial guess [40] (Pg. 31, Prop. 2.18). □

Lemma 5.2. *At each time step n, the sequence $\{W^{n,(m)}\}_m$ generated by (37) converges quadratically to the solution W^n of (36) for an appropriate initial guess.*

Proof. The Jacobian in (37)(b) is given by

$$\mathbb{J}_\beta^{n,(m-1)} = \mathscr{M} + \tau_n\mathscr{A}\mathscr{J}_\beta^{n,(m-1)} = \left(I + \tau_n\mathscr{A}\mathscr{J}_\beta^{n,(m-1)}\mathscr{M}^{-1}\right)\mathscr{M}. \tag{39}$$

Since $\mathscr{A}\mathscr{J}_\beta^{n,(m-1)}\mathscr{M}^{-1}$ in (39) is not symmetric, we cannot proceed as in the proof of Lemma 5.1.

Since $\mathscr{A}$ is symmetric positive semidefinite and $\mathscr{J}_\beta^{n,(m-1)}\mathscr{M}^{-1}$ is diagonal with non-negative entries from Lemma 2.1 and (17), the product $\mathscr{A}\mathscr{J}_\beta^{n,(m-1)}\mathscr{M}^{-1}$ has non-negative eigenvalues. Hence $\lambda\left(I + \tau_n\mathscr{A}\mathscr{J}_\beta^{n,(m-1)}\mathscr{M}^{-1}\right) \geq 1$, and consequently $\left(I + \tau_n\mathscr{A}\mathscr{J}_\beta^{n,(m-1)}\mathscr{M}^{-1}\right)$ is invertible. Since $\mathbb{J}_\beta^{n,(m-1)}$ in (39) is a product of two invertible matrices, it is invertible.

We now apply a result from literature to prove the uniform boundedness of $\left\|\left(\mathbb{J}_\beta^{n,(m-1)}\right)^{-1}\right\|_1$. Since $\mathscr{A}$ is symmetric and weakly diagonally dominant (see Appendix A.2), the product $\mathscr{A}\mathscr{J}_\beta^{n,(m-1)}\mathscr{M}^{-1}$ is also column-wise weakly diagonally dominant since right multiplication of a matrix by a diagonal matrix scales the columns of the former by the diagonal entries of the latter. Hence from Lemma A.1 we have

$$\left\|\left(\mathbb{J}_\beta^{n,(m-1)}\right)^{-1}\right\|_1 \leq \left\|\mathscr{M}^{-1}\right\|_1 \left\|\left(I + \tau_n\mathscr{A}\mathscr{J}_\beta^{n,(m-1)}\mathscr{M}^{-1}\right)^{-1}\right\|_1 \leq \left\|\mathscr{M}^{-1}\right\|_1 \leq \frac{1}{h_{min}^2}. \tag{40}$$

Finally, since β is order-1 semismooth, we see that the sequence $\{W^{n,(m)}\}_m$ converges quadratically for an appropriate initial guess [40] (Pg. 31, Prop 2.18). □

5.3. Local convergence of P0-P0-Θ and P0-P0-W

In Lemmas 5.1 and 5.2 we showed local convergence of our nonlinear P0-P0 solvers P0-P0-Θ and P0-P0-W for an appropriate initial guess regardless of which primary variable is used (temperature or enthalpy). Now we compare their performance, with focus on the magnitude of the time step that guarantees convergence.

We recall that when using the semismooth Newton's method to seek a solution S_* to $g(S) = 0$, for some $g : \mathbb{R}^I \to \mathbb{R}^I$, convergence is guaranteed if the initial guess S_0 is in a neighborhood $B_{r_0}(S_*)$, where $r_0 > 0$ is such that $\forall \delta S,\ \|\delta S\| < r_0$, we have

$$\left\|g(S + \delta S) - g(S) - \mathscr{J}_g \delta S\right\|_q \leq (2C)^{-1}\|\delta S\|_q,\ \ \mathscr{J}_g \in \partial g(S + \delta S), \tag{41}$$

with $C > 0$ being the uniform upper bound of the Jacobian $\|\mathscr{J}_g^{-1}\|_q \leq C$ [40] (Prop. 2.7, Eq. (2.1)), and $q \in \{1, 2\}$.

In the temperature formulation (33), the nonlinearity is $g = \alpha^P$. For the linear part of α^P, the left hand side of (41) equals 0, but near $\theta < \theta_*$, from (11) $(\alpha^P)'$ is large for SFCs with steep gradients, i.e., large $L_{\chi_l^P}$. Hence, in such cases, we anticipate r_0 to be small for (41) to hold near $\theta \approx \theta_*$. That is, convergence would be guaranteed only if the initial guess is really close to the solution, or equivalently, we would only expect P0-P0-Θ to converge for small time steps.

On the other hand, in the enthalpy formulation (36), the nonlinearity is $g = \beta^P$. In this case, by (15), $(\beta^P)'$ remains bounded independently of $L_{\chi_l^P}$. In fact, $(\beta^P)'$ decreases near $w \approx w_*$ as $L_{\chi_l^P}$ increases. Thus we do not need r_0 to be too small for (41) to hold, and we expect P0-P0-W would converge for large time steps.

We illustrate these observations through numerical tests in Sections 6.2 and 6.3.

Table 3
Parameters used in Example 6.1.

c_i, c_l, c_r	k_i, k_l, k_r	L	θ_*
1	1	1	0

Table 4
Results for Example 6.1.

Case	τ	$\|\theta_{err}\|_{\infty,2}$	$\|\theta_{err}\|_{\infty,1}$	$\|\theta_{err}\|_{2,2}$	$\|w_{err}\|_{\infty,2}$	$\|w_{err}\|_{\infty,1}$	$\|w_{err}\|_{2,2}$	$\|q_{err}\|_{\infty,2}$	$\|q_{err}\|_{\infty,1}$	$\|q_{err}\|_{2,2}$
(ST)	$O(h)$	1.25	1.33	1.23	0.51	1.01	0.50	0.51	0.97	0.50
	$O(h^2)$	1.22	1.44	1.23	0.50	1.01	0.49	0.40	0.78	0.50
(P)	$O(h)$	1.29	1.28	1.11	1.33	1.18	1.11	1.21	1.24	1.16
	$O(h^2)$	1.85	1.99	1.85	1.85	2.00	1.84	1.25	1.50	1.24

6. Numerical experiments

In this section, we provide numerical experiments to demonstrate the performance of our P0-P0 algorithm as well as the features of P0-P0-Θ and P0-P0-W solvers. We start with tests of convergence to verify the theoretical estimates from Section 4. Next, we provide physical permafrost scenarios to test the robustness of our algorithms when handling different SFCs, boundary conditions, and media heterogeneity.

6.1. Order of convergence

We now provide convergence studies for permafrost models using our P0-P0-Θ algorithm. Similar tests were given in [12] for the Stefan problem and θ, w variables.

Here we give the errors for θ, w, and q and in the $\|\cdot\|_{\infty,2}, \|\cdot\|_{\infty,1}$ and $\|\cdot\|_{2,2}$ error norms (see Appendix A.4 for their details). We estimate the orders of convergence using two examples: one with a known analytical solution and another with a fine grid solution.

For the first example, we consider a non-physical scenario with a known analytical solution adapted from [17] (Example 1). We provide the convergence orders obtained for the Stefan problem using P0-P0-W.

Example 6.1. Let $\Omega = (0, 0.4) \times (0, 0.2)$ and $S(x,t) = 0$, $S(x,t) = -x + t + 0.1$, be the free boundary between the frozen and thawed states, with material parameters as in Table 3. In the first case, we consider the Stefan problem with analytical solution [17] (Example 1)

$$w^{ST} = \begin{cases} e^S - 1; & S < 0 \\ 2(e^S - 1) + 1; & S \geq 0, \end{cases} \quad \theta^{ST} = \begin{cases} e^S - 1; & S < 0 \\ 2(e^S - 1); & S \geq 0, \end{cases} \quad q^{ST} = \begin{cases} e^S; & S < 0 \\ 2e^S; & S \geq 0, \end{cases} \tag{42}$$

and external source $f^{ST} = 0$. For the second case, we modify (42) to satisfy the permafrost model. We choose the adapted M SFC with parameters $b^M = 2, \chi^M_{res} = 0, \theta^M_* = 0$, and a porosity of $\eta = 0.5$. The thermal parameters of the rock material are as in Table 3. The analytical solution is given by

$$\theta^P = \begin{cases} e^{2S} - 1; & S < 0 \\ 2(e^S - 1); & S \geq 0, \end{cases} \quad w^P = \begin{cases} (e^{2S} - 1) + 0.5e^{2(e^{2S}-1)}; & S < 0 \\ 2(e^S - 1) + 0.5; & S \geq 0, \end{cases} \quad q^P = \begin{cases} 2e^{2S}; & S < 0 \\ 2e^S; & S \geq 0, \end{cases} \tag{43a}$$

with the external source term

$$f^P = \begin{cases} 2\left[e^{2(e^{2S}-1)} - 1\right] e^{2S}; & S < 0 \\ 0; & S \geq 0. \end{cases} \tag{43b}$$

It is worthwhile to note that

$$[q^{ST}]_{S=0} = 2 - 1 = 1 = L \frac{\partial S}{\partial t}\Big|_{S=0}, \tag{44a}$$

however

$$[q^P]_{S=0} = 2 - (2) = 0. \tag{44b}$$

This difference is in accordance with the fact that $q^P \in H_{div}$ but $q^{ST} \notin H_{div}$.

We obtain the errors using grid sizes $h \in \{2, 1, 0.5\} \times 10^{-3}$ and $\tau = (1.25 \times 10^{-1})h$ and $\tau = (1.5625 \times 10)h^2$. The convergence rates are tabulated in Table 4. We seek the order p of the error $O(h^p)$.

For the permafrost model, we obtain at least $p \approx 1$ for θ, w, and q when using $\tau = O(h)$; when $\tau = O(h^2)$, we obtain order $p \in [1.8, 2]$ for θ, w, and order $p \in [1.25, 1.5]$ for q. In contrast, for the Stefan problem, $p \approx 1$ for θ and $p \approx 0.5$ for w and q regardless

Table 5
Thermal parameters of water and rock grains used in this paper.

Material	c [J/m^3 °C]	k [J/m s °C]	L [J/m^3]	θ_* [°C]	Ref.
Liquid water	4.19×10^6	0.58	306×10^6	0	[32] (Section 4)
Ice	1.90×10^6	2.30	306×10^6	0	[32] (Section 4)
Rock grains	2.36×10^6	1.95	0	0	[6] (Table 1)

Table 6
Results of Examples A.1 and 6.2. Orders of convergence are obtained using fine grid solution with $h^{fine}=2\times10^{-3}$ [cm] and $\tau^{fine}=1$ [s].

Model	τ	$\|\theta_{err}\|_{\infty,2}$	$\|\theta_{err}\|_{\infty,1}$	$\|\theta_{err}\|_{2,2}$	$\|w_{err}\|_{\infty,2}$	$\|w_{err}\|_{\infty,1}$	$\|w_{err}\|_{2,2}$	$\|q_{err}\|_{\infty,2}$	$\|q_{err}\|_{\infty,1}$	$\|q_{err}\|_{2,2}$
Example 6.2(i)										
L	$O(h)$	0.97	0.97	0.96	0.96	0.96	0.95	0.76	1.00	0.92
	$O(h^2)$	2.01	2.01	2.01	2.01	2.01	2.02	1.53	1.98	1.93
W	$O(h)$	0.96	0.96	0.96	0.95	0.95	0.96	0.76	1.00	0.90
	$O(h^2)$	2.01	2.01	2.01	2.01	2.01	2.02	1.53	1.97	1.93
M	$O(h)$	0.96	0.97	0.97	0.98	0.96	0.97	0.76	1.00	0.89
	$O(h^2)$	2.01	2.01	2.01	2.00	2.01	2.02	1.53	1.97	1.94
Example 6.2(ii)										
L	$O(h)$	1.34	1.35	1.40	1.46	1.58	1.34	0.95	1.16	1.04
	$O(h^2)$	1.08	1.27	1.57	1.39	1.89	1.65	1.01	1.15	1.08
W	$O(h)$	1.69	1.55	1.31	1.38	1.34	1.21	1.08	1.33	1.06
	$O(h^2)$	1.60	1.63	1.69	1.56	1.89	1.85	1.16	1.41	1.21
M	$O(h)$	1.52	1.46	1.41	1.55	1.48	1.30	1.05	1.29	1.13
	$O(h^2)$	0.98	1.32	1.63	1.62	1.95	1.85	1.13	1.21	1.22

when $\tau=O(h)$ or $O(h^2)$. The higher orders of convergence in permafrost models is due to the increased regularity of α^P compared to α^{ST}.

We consider next a realistic physical scenario, and compute the order of convergence using fine grid solutions. The permafrost model features a moving thawing front. For reference, we provide the test for the linear heat equation in Example A.1 in Appendix A.3.1.

Example 6.2. Let $\Omega=(0,0.2)$ [m] be occupied by a soil with porosity $\eta=0.55$ and SFC parameters as in Table 7. The thermal properties are taken from Table 5. We choose $w_0=\alpha^P(\theta_0)$ and boundary conditions

$$\theta(0,t)=\theta_0,\ \theta(0.2,t)=\theta_0+\frac{2t}{5000},\ \forall t>0, \tag{45}$$

where (i) $\theta_0=-4$ or (ii) $\theta_0=-1.5$ [°C]. The simulations are run over $t\in(0,5000)$ [s]. We consider grid size $h\in\{0.4,0.2,0.1\}\times10^{-2}$ [m] and time step $\tau=(5\times10^4)h$ [s] and $\tau=(5\times10^7)h^2$ [s]. The results are tabulated in Table 6.

For permafrost models in Example 6.2, in case (i), we obtain order $p=1$ and $p=2$ for θ,w, and q when using $\tau=O(h)$ and $O(h^2)$, respectively. This agrees with the estimate (28) since the problem is only mildly nonlinear, i.e., the nonlinearity α^P is smooth as $\theta(x,t)<\theta_*,\forall(x,t)\in\Omega_T$. In case (ii), however, we obtain orders $p\approx1.2$–1.6 for θ,w and $p\approx1$–1.2 for q, when using $\tau=O(h)$. There is only a slight improvement when using $\tau=O(h^2)$. This is expected since in this case $\theta(x,t)>\theta_*$ for some $(x,t)\in\Omega_T$: about 5% of the domain completely thaws by the end of the simulation. Since α^P is non-smooth for some time of simulation, we can only expect orders in accordance with (26).

Summary: We see that using our P0-P0 scheme for permafrost models we see roughly first order of convergence for both θ,w, and q with $\tau=O(h)$ in all norms. In scenarios not involving phase transition, quadratic order can be obtained as long as $\tau=O(h^2)$. These rates are better than for the Stefan problem, where θ is first order convergent, but w only half [12] (Section 3.4), and results are better for weaker norms.

6.2. Robustness of solvers

In this section, we demonstrate robustness of our P0-P0 solvers for permafrost scenarios with respect to different boundary conditions and domain heterogeneity. In particular, we compare performance of P0-P0-Θ and P0-P0-W solvers and test their robustness.

6.2.1. Robustness in practical homogeneous scenarios

We start by comparing the performance of our P0-P0 algorithms in homogeneous permafrost scenarios with physical data.

Table 7
SFC parameters used in Examples 6.2 and 6.3.

Permafrost model	SFC parameters
Adapted L (9a)	$b = 1.75$ [–], $\theta_* = -1$ [°C]
Adapted W (9b)	$b = 5$ [°C], $\chi_{res} = 0$ [–], $\theta_* = -1$ [°C]
Adapted M (9c)	$b = 1$ [1/°C], $\chi_{res} = 0$ [–], $\theta_* = -1$ [°C]

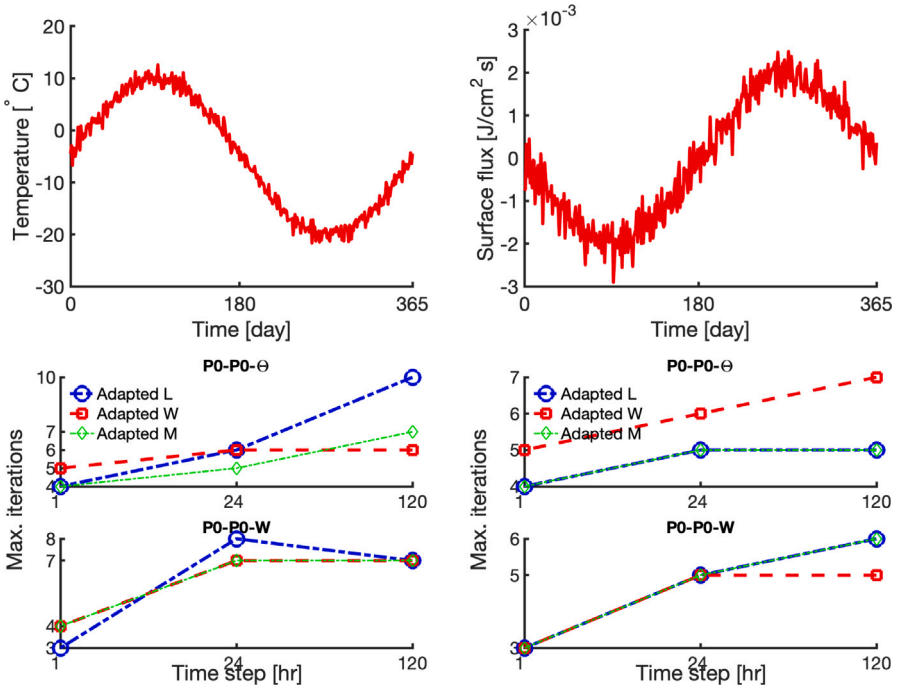

Fig. 4. Illustrations for Example 6.3. Top row: A plot of the surface temperature corresponding to Dirichlet boundary conditions (46a) (left) and surface flux corresponding to Neumann boundary conditions (46b) (right). Bottom row: the maximum number of iterations taken by our P0-P0 algorithms when using Dirichlet (left) and Neumann (right) boundary conditions. Here $h = 10^{-2}$ [m].

Example 6.3. Let $\Omega = (0, 1)$ [m] with porosity $\eta = 0.55$. We consider the SFCs with parameters as in Table 7. We choose initial conditions $\omega_0 = \alpha^P(\theta_0)$ and consider two sets of boundary conditions: (i) Dirichlet boundary conditions

$$\theta(0, t) = -5 + 15 \sin(2\pi t) + \mathcal{N},\ \theta(1, t) = -5\ [°\mathrm{C}],\ \forall t > 0, \tag{46a}$$

and (ii) Neumann boundary conditions

$$q(0, t) \cdot \nu = -0.002 \sin(2\pi t) - 0.0003\mathcal{N},\ q(1, t) \cdot \nu = 0.0001\ [\mathrm{J/cm^2\ s}],\ \forall t > 0, \tag{46b}$$

where $\mathcal{N} \sim N(0, 1)$ is Gaussian noise added to the signal to replicate the oscillatory nature of field measured data; see Fig. 4 for a plot of boundary conditions (46).

The simulation is run over $t \in (0, 1)$ [year]. We choose grid sizes $h \in \{5, 1, 0.2\} \times 10^{-2}$ [m] and $\tau \in \{120, 24, 1\}$ [h]. The results are given in Tables 14–15, and shown in Fig. 4 for $h = 10^{-2}$ [m].

In both the cases of Dirichlet and Neumann boundary conditions, P0-P0-Θ performs robustly for all three SFCs with a maximum of 10 and average of 1.6–3.9 iterations. Further, for large τ, some time step reduction is observed for the adapted L SFC in the Dirichlet case, and for all SFCs in the Neumann case. Moreover, when using P0-P0-W, for all SFCs the maximum and average iterations are reduced to 8 and 1.3–3.4, respectively. More importantly, there was no time step reduction for any SFC.

This example demonstrates that P0-P0-W is more robust than P0-P0-Θ for large time steps.

6.2.2. *Robustness in heterogeneous domains*

The argument in Section 5.3 shows that the rate of convergence of our P0-P0 algorithms depends on the data for which (41) holds, which in turn depends on the SFC. We now test this observation for a heterogeneous SFCs $\chi_l^P = \chi_l^P(x, \theta)$, and demonstrate the robustness of our P0-P0 algorithms in heterogeneous domains.

Consider the stationary system

$$W + A\Theta = F,\ W = \alpha(\Theta), \tag{47}$$

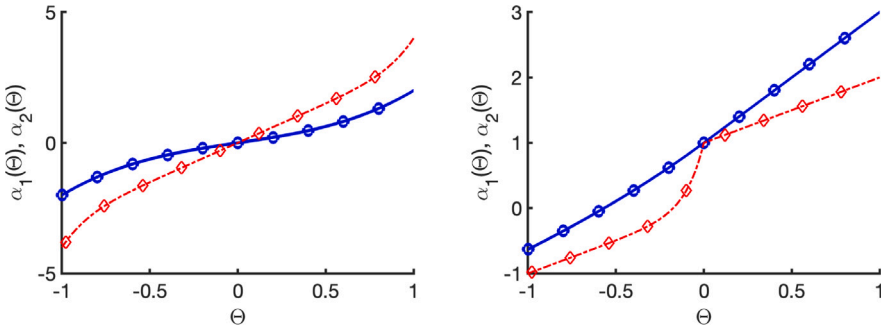

Fig. 5. Illustration for Example 6.4 showing the selected smooth (left) and semismooth (right) functions α_1 and α_2 used to compare the performance of our P0-P0 algorithm. Note the difference in the gradients of the two curves in each plot.

where $W = \begin{bmatrix} W_1 \\ W_2 \end{bmatrix}$, $\Theta = \begin{bmatrix} \Theta_1 \\ \Theta_2 \end{bmatrix} \in \mathbb{R}^2$, $A = \begin{bmatrix} 2k & -k \\ -k & 2k \end{bmatrix}, k > 0$, and $\alpha : \mathbb{R}^2 \to \mathbb{R}^2$, $\alpha(\Theta) = \begin{bmatrix} \alpha_1(\Theta_1) \\ \alpha_2(\Theta_2) \end{bmatrix}$, for some semismooth $\alpha_1, \alpha_2 : \mathbb{R} \to \mathbb{R}$, and $F \in \mathbb{R}^2$ is a constant. The system (47) arises when (22) is written for $N_\omega = 2$ cells; we do not consider (47) to be related to any particular physical scenario.

When using P0-P0-Θ, the Jacobian in (34)(b) is given by $\mathbb{J}_\alpha^{(m-1)} = \mathscr{J}_\alpha^{(m-1)} + A$, where $\mathscr{J}_\alpha^{(m-1)} \in \partial\alpha(\Theta^{(m-1)})$ is given by $\mathscr{J}_\alpha^{(m-1)} = \begin{bmatrix} J_{\alpha_1}^{(m-1)} & 0 \\ 0 & J_{\alpha_2}^{(m-1)} \end{bmatrix}$, $J_{\alpha_j}^{(m-1)} \in \partial\alpha_j(\Theta_j^{(m-1)})$. Now, substituting $g(\Theta) = \alpha(\Theta) + A\Theta$ in the left hand side of (41) gives, with $\delta\Theta = [\delta\Theta_1, \delta\Theta_2]^T$, that

$$\left\|\alpha(\Theta + \delta\Theta) - \alpha(\Theta) - \mathscr{J}_\alpha \delta\Theta\right\|_2 = \left(\sum_{i=1}^{2} \left|\alpha_i(\Theta_i + \delta\Theta_i) - \alpha_i(\Theta_i) - J_{\alpha_i}\delta\Theta_i\right|^2\right)^{1/2}, \; J_{\alpha_i} \in \partial\alpha_i(\Theta_i + \delta\Theta_i).$$

By extending the argument from Section 5.3, if either α_1 or α_2 features a steep gradient, the algorithm P0-P0-Θ requires small time steps for convergence. The performance of P0-P0-Θ is mostly affected by the features of α_1 and α_2 rather than the heterogeneity $\alpha_1(\Theta) \neq \alpha_2(\Theta)$. Similar reasoning applies to P0-P0-W.

We now illustrate the above with a numerical example.

Example 6.4. Consider the system (47). We choose smooth and semismooth expressions for α_1 and α_2 and compute the solution corresponding to a given F using our algorithms. We test P0-P0-Θ and P0-P0-W with respect to different initial guesses Θ_0 and $W_0 = \alpha(\Theta_0)$, respectively, and with respect to different values of k. The expressions of α_1 and α_2 and the value of F are listed in Table 8. We also plot α_1 and α_2 in Fig. 5. The results are given in Table 8.

We see that P0-P0-Θ struggles to converge in cases when α_1 or α_2 has a steep gradient. Further, for semismooth functions, no convergence of P0-P0-Θ is observed when k is small. When using P0-P0-W, however, convergence is achieved for all cases with fewer iterations than P0-P0-Θ.

Summary: Our P0-P0 algorithms appear to perform robustly in heterogeneous permafrost scenarios regardless of the boundary conditions or SFC expressions used. We also see that P0-P0-W performs better than P0-P0-Θ with fewer iterations and time step reductions. In particular, a time step of 1–120 [h] for a grid size of 0.2×10^{-2}–5×10^{-2} [m] appears to suffice for convergence in practical permafrost scenarios.

6.3. Physically realistic simulations

We now test the application of our P0-P0 scheme in heterogeneous permafrost scenarios with physical data. First, in Section 6.3.1, we consider heterogeneity, i.e., multiple soil types, with data measured in Alaska. Next, in Section 6.3.2 we consider heterogeneity due to an ice wedge in $d = 1$ and $d = 2$. We see that our P0-P0 algorithms apply well in such scenarios, and we reconfirm the advantages of P0-P0-W over P0-P0-Θ.

6.3.1. Utqiagvik, Alaska

In this example, we use the data measured at Utqiagvik, Alaska (formerly known as Barrow). The data is taken from Permafrost Laboratory, University of Alaska, Fairbanks [61], and the Circumpolar Active Layer Monitoring Program [62,63]. The purpose of our simulation is not to exactly replicate the measured temperature values but to show the robustness of our algorithms when handling heterogeneity and physical data. For that reason, we ignore additional factors such as the dependence of the thermal soil properties on the temperature or the effects of snow on the ground surface.

Data description and calibration: At Utqiagvik, we use data from two different sites: water fraction data from NGEE Barrow C and ground surface temperature from Barrow 2 (N. Meadow Lake No. 2/NML-2) [61]; see Fig. 6 for a plot of the ground surface

Table 8
Results for Example 6.4 show that the performance of our P0-P0 algorithm appears to depend on the steepness of gradient of α_1 or α_2 rather than the heterogeneity represented by $\alpha_1(\Theta) \neq \alpha_2(\Theta)$.

$\alpha_1(\Theta)$	$\alpha_2(\Theta)$	F	k	Θ_0	P0-P0-Θ	P0-P0-W
Smooth functions					Convergence?/Iter.	Convergence?/Iter.
$\Theta^3+\Theta$	$\Theta^3+\Theta$	$[1.5\ 1]^T$	1	$[1\ 1]^T$	Yes/4	Yes/4
				$[6\ 5]^T$	Yes/7	Yes/5
			10^{-3}	$[1\ 1]^T$	Yes/4	Yes/2
				$[6\ 5]^T$	Yes/7	Yes/2
$\Theta^3+\Theta$	$\Theta^7+3\Theta$	$[1.5\ 1]^T$	1	$[1\ 1]^T$	Yes/4	Yes/3
				$[6\ 5]^T$	Yes/12	Yes/4
			10^{-3}	$[1\ 1]^T$	Yes/4	Yes/2
				$[6\ 5]^T$	Yes/12	Yes/1
$\Theta^7+3\Theta$	$\Theta^7+3\Theta$	$[1.5\ 1]^T$	1	$[1\ 1]^T$	Yes/4	Yes/3
				$[6\ 5]^T$	Yes/13	Yes/3
			10^{-3}	$[1\ 1]^T$	Yes/4	Yes/2
				$[6\ 5]^T$	Yes/13	Yes/1
Semismooth functions						
$\begin{cases}\Theta+e^{\Theta}; & \Theta<0\\ 2\Theta+1; & \Theta\geq 0\end{cases}$	$\begin{cases}\Theta+e^{\Theta}; & \Theta<0\\ 2\Theta+1; & \Theta\geq 0\end{cases}$	$[0.98\ 0.95]^T$	1	$[-2\ -2.5]^T$	Yes/3	Yes/3
				$[3\ 2]^T$	Yes/2	Yes/2
			10^{-3}	$[-2\ -2.5]^T$	Yes/3	Yes/2
				$[3\ 2]^T$	Yes/2	Yes/1
$\begin{cases}\Theta+e^{\Theta}; & \Theta<0\\ 2\Theta+1; & \Theta\geq 0\end{cases}$	$\begin{cases}\Theta+e^{10\Theta}; & \Theta<0\\ \Theta+1; & \Theta\geq 0\end{cases}$	$[0.98\ 0.95]^T$	1	$[-2\ -2.5]^T$	Yes/5	Yes/4
				$[3\ 2]^T$	Yes/4	Yes/3
			10^{-3}	$[-2\ -2.5]^T$	No	Yes/2
				$[3\ 2]^T$	No	Yes/2
$\begin{cases}\Theta+e^{10\Theta}; & \Theta<0\\ \Theta+1; & \Theta\geq 0\end{cases}$	$\begin{cases}\Theta+e^{10\Theta}; & \Theta<0\\ \Theta+1; & \Theta\geq 0\end{cases}$	$[0.98\ 0.95]^T$	1	$[-2\ -2.5]^T$	Yes/5	Yes/4
				$[3\ 2]^T$	Yes/4	Yes/3
			10^{-3}	$[-2\ -2.5]^T$	No	Yes/2
				$[3\ 2]^T$	No	Yes/2

Table 9
SFC parameters used in Example 6.5. Here we use the adapted L SFC given by (9a).

Subdomain	SFC parameters
$\Omega^{(1)}=(0,0.2)$ [m]	$b=0.42, \theta_*=-0.002, \eta=0.56$
$\Omega^{(2)}=(0.2,0.4)$ [m]	$b=0.81, \theta_*=-0.03, \eta=0.46$
$\Omega^{(3)}=(0.4,40)$ [m]	$b=1.43, \theta_*=-0.05, \eta=0.51$

temperature. The two sites are roughly 3.8 [km] apart and have available recorded data from 2012–2018. The yearly active layer depth data is taken from [62,63] Barrow CRREL plots from 2013–2018 which is measured between mid August to September, when the thaw depth is the maximum [62] (Pg. 169).

We calibrate the adapted L SFC using the available daily water fraction data from 2012–2013 at depths of $0.15, 0.30$, and 0.42 [m]. The obtained SFC parameters are tabulated in Table 9.

Example 6.5. Let $\Omega=(0,40)$ [m] be partitioned into subdomains $\Omega^{(1)}=(0,0.2), \Omega^{(2)}=(0.2,0.4)$, and $\Omega^{(3)}=(0.4,40)$, where each $\Omega^{(j)}, 1\leq j\leq 3$ is occupied with a soil type with SFC parameters as in Table 9. We use Dirichlet boundary conditions at $x=0$ corresponding to the available surface temperature data from $06/01/2013-06/01/2018$ and Neumann boundary conditions

$$q(40,t)\cdot\nu=-0.0565\ [\mathrm{J/m^2\ s}],\ \forall t>0, \tag{48}$$

corresponding to the constant geothermal flux [28].

We choose a non-uniform grid with grid size $h=10^{-2}$ [m] in $(0,2)$ [m] and $h=0.2$ [m] in $(2,40)$ [m], and an initial time step of $\tau=24$ [h].

An interesting question concerns an initial condition, since it should reflect a physically realistic distribution. We calculate the initial condition by using the surface temperature from 06/01/2012–06/01/2013 by following a procedure similar to [28]: we first choose a uniform initial temperature profile -9 [°C] and compute the steady state solution by using the Dirichlet surface temperature value on 06/01/2012 and Neumann condition (48). Using the steady state solution as an initial condition, we further simulate the temperature profile at the end of 3 years by periodically extending the surface temperature data from 06/01/2012–06/01/2013 and using it as the Dirichlet surface boundary condition along with the Neumann condition (48). The temperature

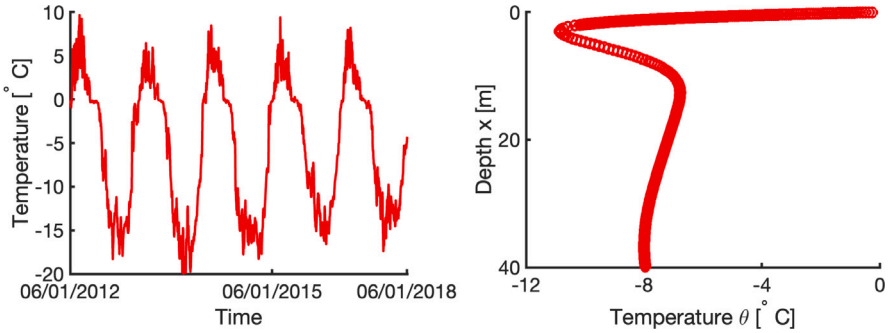

Fig. 6. Illustration for Example 6.5 showing the measured ground surface temperature (left) and the initial temperature profile (right) used in the simulation.

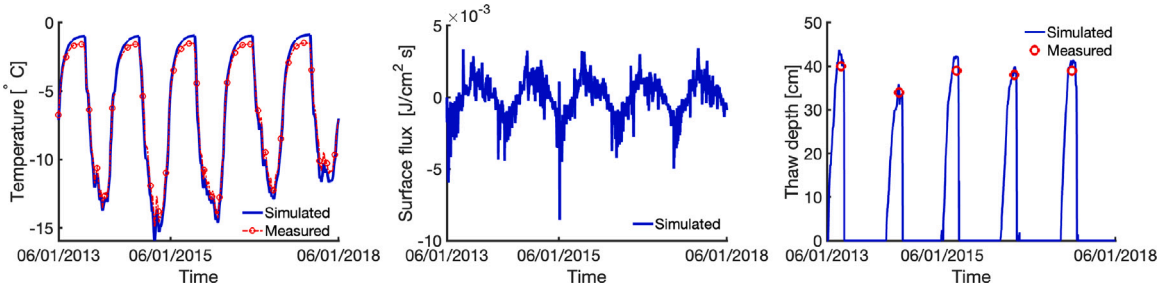

Fig. 7. Results for Example 6.5. Measured and simulated temperature at a depth of approximately 1 [m] (left), simulated flux at the ground surface (middle), and simulated and measured thaw depth (right).

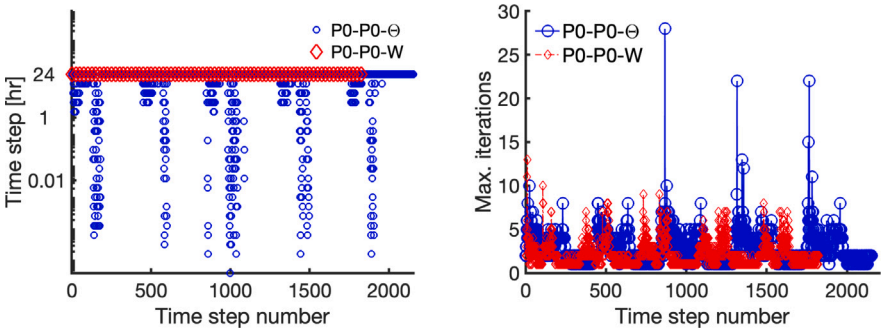

Fig. 8. Performance of our P0-P0 algorithms in Example 6.5. Left: when P0-P0-Θ is used, the time step is reduced even down to $O(10^{-2})$ [s], whereas using P0-P0-W requires no time step reduction. Right: iteration counts show that P0-P0-W takes fewer iterations than P0-P0-Θ for convergence.

profile at the end of the 3 year simulation is shown in Fig. 6: we choose this to be our initial temperature profile for the simulation from 01/06/2013–06/01/2018.

We first run the simulation with P0-P0-Θ solver. At the end of the simulation, we compare the measured and simulated temperature at a depth of 1 [m]. The results are shown in Fig. 7. A maximum difference of $\max_t |\theta^{simulated}(t) - \theta^{measured}(t)| \approx 1.13$ [°C] was obtained at a depth of $x \approx 1$ [m]. We also compute the location of the 0 [°C] isotherm to compute the maximum thaw depth. A good qualitative agreement was observed between the measured and simulated values; see Fig. 7.

We now discuss the performance of the solvers in this challenging case with heterogeneity of the soil and the quickly varying surface temperature data. Fig. 8 shows the time step reduction and iteration count during the simulation.

For P0-P0-Θ solver, the time step is reduced to a minimum of $\tau = 0.04$ [s]. With this reduction, maximum of 28 iterations were taken throughout the simulation, with an average of 2.7.

We next re-run the simulation using P0-P0-W. Now there are only 13 maximum iterations, with average 2.0. Most importantly, there is no time step reduction during the simulation; see Fig. 8.

Table 10
SFC and thermal parameters used in Example 6.6. Here we use the adapted L SFC given by (9a). A plot of the SFCs is shown in Fig. 9.

Soil type	SFC and thermal parameters	Reference
Organic mineral mixture	$b = 0.6, \theta_* = -0.05,\ \eta = 0.50$	[24] (Table 1)
	$c_r = 1.750 \times 10^6$ [J/m^3 °C], $k_r = 0.692$ [J/ms °C]	[25] (Table A.3)
Mineral	$b = 0.5, \theta_* = -0.1,\ \eta = 0.40$	[24] (Table 1)
	$c_r = 2.385 \times 10^6$ [J/m^3 °C], $k_r = 2.92$ [J/ms °C]	[4] (Pg. 90, Table 4.1)

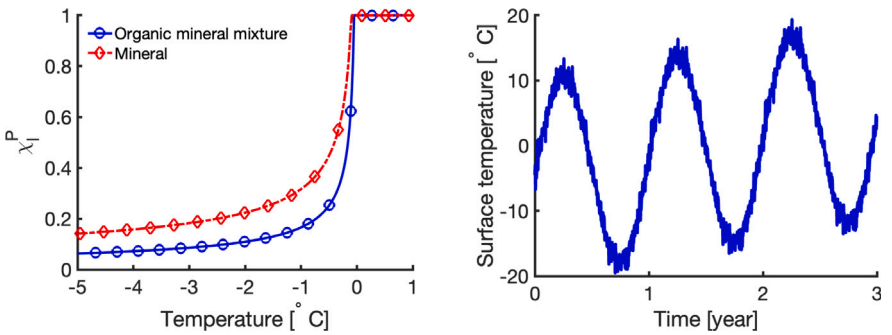

Fig. 9. Illustration for Example 6.6. Left: SFCs of the different soil types used in the example. The parameters are taken from Table 10. Right: the surface temperature (49) used in the simulation clearly showing the warming trend.

6.3.2. Ice wedge modeling

In this example, we model the inclusion of ice and rock wedges in permafrost. We begin with a $d = 1$ example with an ice wedge modeled with different approaches discussed in Section 2.2.1. Next we continue with a $d = 2$ example replacing the ice wedge with a soil, or with solid rock.

Example 6.6. Let $\Omega = (0, 2)$ [m]. Let $\Omega^{(1)} = (0, 0.2)$ be occupied by an organic mineral soil mixture, $\Omega^{(2)} = (0.2, 1.5)$ be occupied by ice, and $\Omega^{(3)} = (1.5, 2)$ be occupied by a mineral soil. The SFCs and thermal parameters are listed in Table 10 and shown in Fig. 9. We choose an initial condition corresponding to $\theta_0 = -5$ [°C] and boundary conditions

$$\theta(0, t) = \theta_s(t) + 3t,\ \theta(2, t) = -5,\ \forall t > 0, \tag{49}$$

where θ_s is the surface temperature (46a) (periodically extended over 3 years) and $3t$ represents an additional warming scenario. A plot of the surface temperature (49) is shown in Fig. 9.

The simulation is run over $t \in (0, 3)$ [year] (1 [year] = 365 [day]) using different grid sizes $h \in \{1.25, 2.5, 5\} \times 10^{-2}$ [m] and time steps $\tau \in \{120, 24, 1\}$ [h]. With P0-P0-Θ, we consider the two approximations $\widetilde{\alpha^{ST}} = \widetilde{\alpha}, \alpha^P$ shown in Fig. 3. We distinguish the corresponding numerical solutions by appropriate superscripts; e.g., $\theta^{\widetilde{\alpha}}$ denotes the temperature obtained using P0-P0-Θ with $\widetilde{\alpha^{ST}} = \widetilde{\alpha}$ and $\theta^{\beta^{ST}}$ using P0-P0-W.

The temperature and water fraction profiles at $t \approx 0.25, 1.25$ and 2.25 [year] are shown in Fig. 10 when using $h = 1.25 \times 10^{-2}$ [m]. A maximum thaw depth of ≈ 0.53 [m] was observed at the end of the simulation. The thawing front is captured most accurately by P0-P0-W, since no regularization or approximation of χ_l^{ST} is used in this case. Comparing to P0-P0-Θ, a maximum difference of $\max_x |\theta^{\alpha^P}(x, t) - \theta^{\beta^{ST}}(x, t)| \approx 0.12$ [°C] and $\max_x |\theta^{\widetilde{\alpha}}(x, t) - \theta^{\beta^{ST}}(x, t)| \approx 0.77$ [°C] occurred near ground surface at $x = 0$ and at $t \approx 2.25$ (the time of the maximum ground surface temperature). We conclude that α^P and $\widetilde{\alpha}$ serve as an effective and accurate approximation of χ_l^{ST} when used in soil-ice wedge scenarios.

We now compare the performance of the solvers for this complex case. Table 11 shows that with P0-P0-Θ, the approximations α_l^P and $\widetilde{\alpha}$ perform similarly. For α^P a maximum of 19 and average of 2.1–4.1 iterations are taken, whereas for $\widetilde{\alpha}$ a maximum of 26 and average of 1.6–1.9 iterations are taken. Further, time step reductions were observed down till $O(10^{-1})$ [s] for α^P and $O(1)$ [s] for $\widetilde{\alpha}$. This is expected due to the high gradients of the approximations α^P and $\widetilde{\alpha}$. However, when using P0-P0-W, a maximum of 9 and average of 1.5–3.2 iterations are taken. Further, time step reduction was only observed for the high value of $\tau_0 = 120$; even then the time step was only reduced till $O(10)$ [h].

Finally we consider a 2D example for ice wedge modeling. We focus on the features of heterogeneity, thus we use constant rather than time-varying boundary conditions. The example is designed to show how easy it is to consider different scenarios, geometries, and rock types with our robust P0-P0 algorithms. In fact, we are able to model the ice domain as (5) with α^P, k^P given with $\eta = 1$, and the solid rock domain with $\eta = 0, L = 0$.

Example 6.7. Let $\Omega = (0, 1) \times (0, 1.2)$ [m^2] be partitioned to three material subdomains shown in Fig. 11 (top left), with the layout summarized in Table 12. The subdomains $\Omega^{(1)}$ and $\Omega^{(3)}$ are occupied by soil types S1 and S2. For $\Omega^{(2)}$, we consider three different

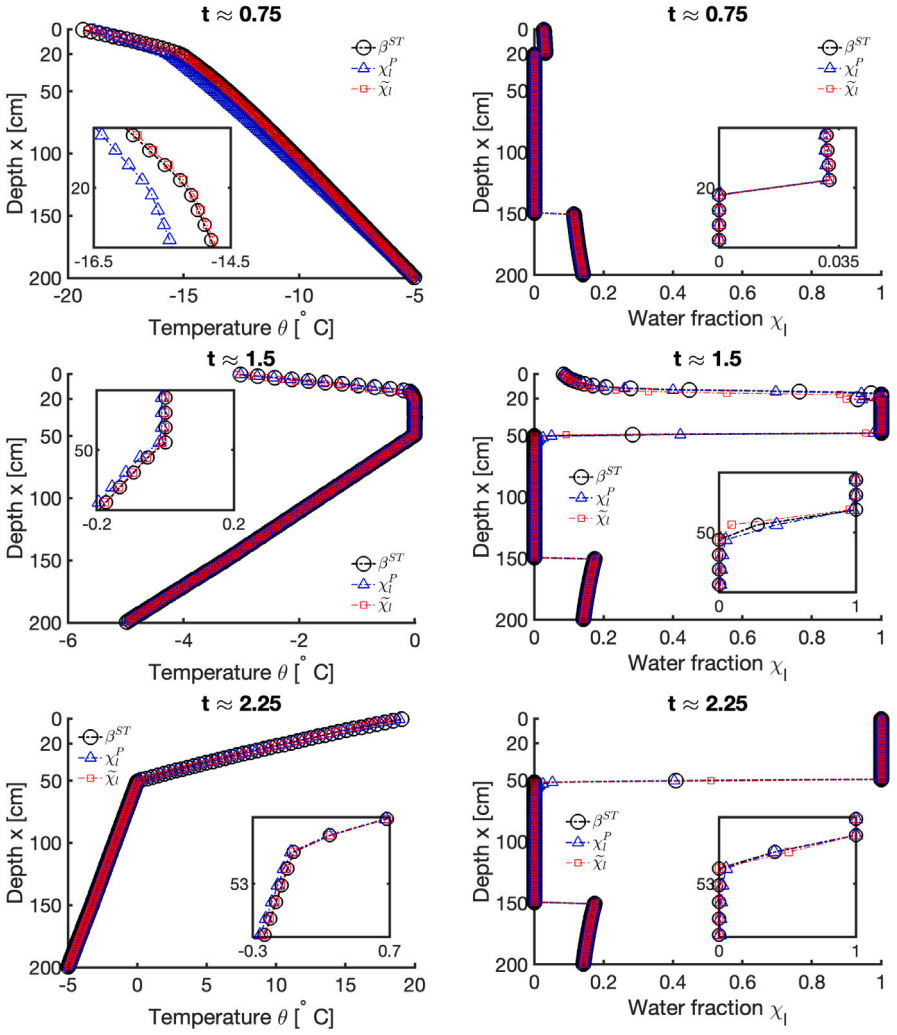

Fig. 10. Results for Example 6.6 showing the temperature (left) and water fraction (right) at different times corresponding to the different model approximations to the ice wedge. Here $h = 1.25 \times 10^{-2}$ [m].

scenarios. The ice wedge case (A) features ice in $\Omega^{(2)}$, with $\eta = 1$ (no rock). This case is compared to (B) where soil type 2 is assigned to $\Omega^{(2)}$, and case (C) when $\Omega^{(2)}$ is occupied by solid rock (e.g., a boulder) with $\eta = 0, b = 0, L = 0, \eta_{res} = 0$. The thermal parameters for all materials are in Table 5, and the SFC using model M (9c) in Table 12.

We consider constant initial conditions $\theta_{init} = -10$ [°C] and a constant Dirichlet boundary condition $\theta = 10$ on $y = 1.2$. On the boundaries $x = 0$, $x = 1$, and $y = 1.2$ we consider the no-flux conditions $q \cdot \nu = 0$. We choose a spatial grid of 100×120 elements and a time step $\tau = 12$[h]. We use θ as a primary unknown, since the case is only mildly challenging.

The simulation is run over $t \in (0, 1)$ [year], with results presented in Figs. 11–12.

The plots in Figs. 11–12 show complex profiles of evolving θ and water fraction χ_l. We see that θ is continuous across material interfaces, but that the water fraction χ_l features a sharp contrast across material interfaces. In addition, as expected, the ice wedge in case (A) thaws the slowest, while $\chi_l|_{\Omega^{(2)}}$ is meaningless in case C and is not plotted.

As concerns solver, the solver P0-P0-Θ is quite robust for this general $d = 2$ case. With the time steps of half-day chosen for accurate dynamics, the solver requires only about 2-4 iterations and no time step cutting. After thawing is initiated, the time step can easily be increased. We do not report more details for brevity.

Summary: The numerical experiments provided in this section further demonstrate the robustness of our P0-P0 algorithms in practical heterogeneous domains. As observed in Section 6.2, we see that P0-P0-W converges with fewer iterations and minimal time step reductions when compared to P0-P0-Θ. However, it requires additional iterations of Ridder's iteration per each cell. This set-up due to its robustness may be more advantageous especially for large domains where the cost of linear solver needed in each iteration of P0-P0-Θ easily outweighs the cost of Ridder's iterations.

Table 11
Results for Example 6.6 comparing the performance of our P0-P0 algorithms. Note that P0-P0-W takes fewer iterations than P0-P0-Θ and converges for larger time steps.

Ice wedge model	h [cm]	τ [h]	Max/min/mean iter.	τ reduced?
P0-P0-Θ				
χ_l^P, α^P	5	120	13/1/3.7	$\tau \approx 0.41$ [s]
		24	9/1/3.0	$\tau \approx 0.65$ [s]
		1	4/1/2.1	$\tau \approx 0.87$ [s]
	2.5	120	9/1/3.9	$\tau \approx 1.6$ [s]
		24	13/1/3.3	$\tau \approx 1.3$ [s]
		1	4/1/2.3	$\tau \approx 1.7$ [s]
	1.25	120	18/1/4.1	$\tau \approx 0.41$ [s]
		24	19/1/3.5	$\tau \approx 1.3$ [s]
		1	4/1/2.4	$\tau \approx 1.7$ [s]
$\widetilde{\chi}_l, \widetilde{\alpha}$	5	120	11/1/1.9	$\tau \approx 13.1$ [s]
		24	7/1/1.9	$\tau \approx 5.2$ [s]
		1	4/1/1.6	$\tau \approx 3.5$ [s]
	2.5	120	26/1/1.9	$\tau = 6.5$ [s]
		24	7/1/1.9	$\tau \approx 5.2$ [s]
		1	4/1/1.7	$\tau \approx 7.0$ [s]
	1.25	120	16/1/1.8	$\tau \approx 3.2$ [s]
		24	9/1/1.9	$\tau \approx 5.2$ [s]
		1	4/1/1.7	$\tau = 1.7$ [s]
P0-P0-W				
χ_l^{ST}, β^{ST}	5	120	8/1/2.5	No
		24	6/1/1.8	No
		1	3/1/1.5	No
	2.5	120	8/1/2.8	$\tau = 60$ [h]
		24	8/1/2.0	No
		1	4/1/1.5	No
	1.25	120	9/1/3.2	$\tau = 30$ [h]
		24	9/1/2.2	No
		1	4/1/1.5	No

Table 12
Definition of Cases A–B–C in Example 6.7, with SFC parameters used in the adapted M model given by (9c). Top: data. Bottom: simulation results for Example 6.7.

Material	η	L	θ_{res}	b
S1	0.5	L_w	0.21	0.16
S2	0.2	L_w	0.21	0.16
Ice wedge	1	L_w	0.01	2
Solid rock	0	0	0	0

Case	$\Omega^{(1)}$, $\Omega^{(2)}$, $\Omega^{(3)}$	Min,Max$_{x\in\Omega}\chi(x,T)$	Newton iter.
A	S1,Ice,S2	0,1	4(5).
B	S1,S2,S2	0.2986,1	3(5)
C	S1,Rock,S2	0.3114,1	4(5)

7. Summary and conclusions

In this paper we presented and analyzed a robust algorithm to model heat conduction in permafrost scenarios based on lowest order mixed finite elements and the semismooth Newton's solver. We demonstrated convergence and tested its robustness for realistic permafrost applications.

In particular, we verified the optimal order of convergence of our schemes as suggested by the literature results for similar problems.

We also investigated the advantages of the enthalpy formulation over the temperature formulation, with two variants of nonlinear solver, respectively, called P0-P0-Θ and P0-P0-W. We proved their convergence based on the analysis of the properties of the nonlinear temperature–enthalpy relationships α^P and its inverse, β^P. In the end, the algorithm P0-P0-W using enthalpy as primary unknown is more robust, but it requires an additional local nonlinear solver. However it (i) does not require any regularization of α, even in scenarios involving SFCs with steep gradients or ice wedges, and it (ii) converges for large time steps.

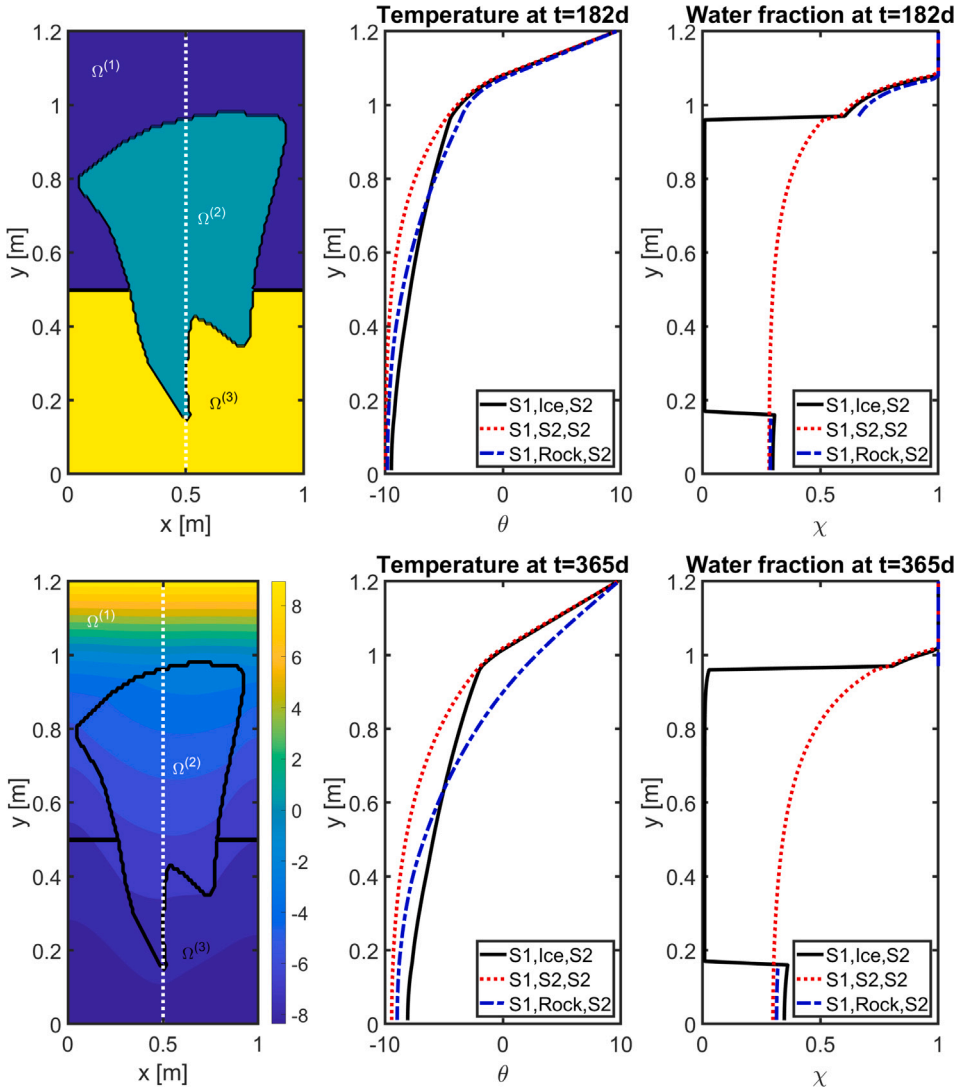

Fig. 11. Simulation set-up and results for Example 6.7. Left column: sketch of the domains (top), and temperature plot for case (A). Middle and right columns: $\theta(0.5, y, t), \chi_l(0.5, y, t)$ at $t = 1$[y] (top), and $t = 0.5$[y] (bottom) for cases A, B, C.

We further demonstrated robustness of our P0-P0 algorithms in different permafrost scenarios including those with extreme heterogeneity due to multiple soil types or ice or rock wedges. Moreover, our P0-P0 algorithms are conservative and consistent in contrast to other schemes frequently used in literature which employ the "apparent heat capacity technique".

Data availability

We use publicly available data and scientific articles in examples in the paper. As for software, we plan to make portions of the code available upon request on Peszynska's website.

Acknowledgments

This research was partially supported by National Science Foundation DMS-2309682 "Computational mathematics of Arctic processes", National Science Foundation DMS-1912938 "Modeling with Constraints and Phase Transitions in Porous Media", and National Science Foundation DMS-1522734 "Phase transitions in porous media across multiple scales". PI: Malgorzata Peszynska. The authors would also like to acknowledge helpful discussions with Dr Lisa Bigler, co-author on our related work in [12,13].

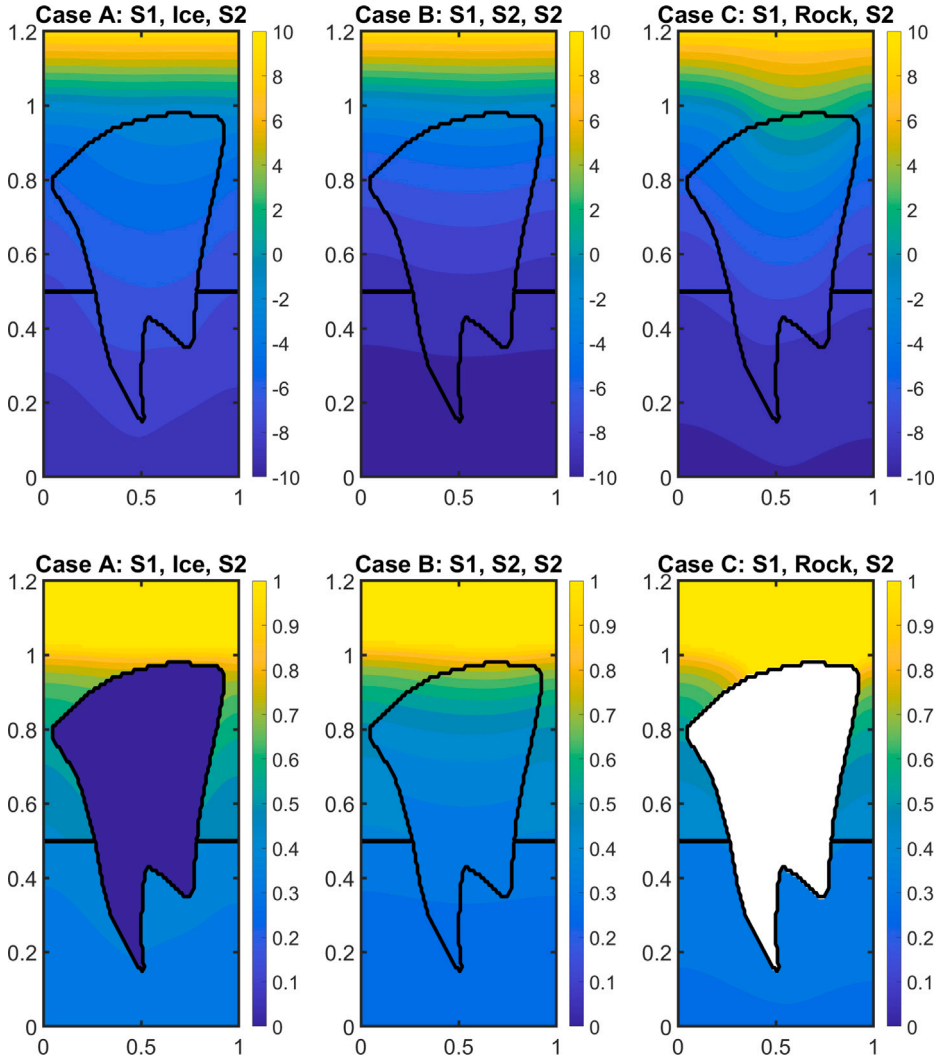

Fig. 12. Simulation results for Example 6.7. Profiles of θ (top), and χ (bottom) at $t = 1$[y]. Visible is continuity of temperature, and discontinuity of water fraction.

Appendix

A.1. Weighting of k_r, k_l, k_i in k^P

To obtain $k^P(x,\theta)$, one has to weigh k_r, k_l, k_i depending on the local geometry of pore space or at least the proportions of rock, liquid, and ice within the pores.

In particular, one of the following three expressions can be employed

$$k^A = k_u^A \chi_l^P + k_f^A (1-\chi_l^P),\ k_u^A = \eta k_l + (1-\eta)k_r,\ k_f^A = \eta k_i + (1-\eta)k_r, \tag{50a}$$

$$k^G = (k_u^G)^{\chi_l^P} (k_f^G)^{1-\chi_l^P},\ k_u^G = {k_l}^{\eta} {k_r}^{1-\eta},\ k_f^G = {k_i}^{\eta} {k_r}^{1-\eta}, \tag{50b}$$

$$k^H = \left(\frac{\chi_l^P}{k_u^H} + \frac{1-\chi_l^P}{k_f^H} \right)^{-1}, k_u^H = \left(\frac{\eta}{k_l} + \frac{1-\eta}{k_r} \right)^{-1},\ k_f^H = \left(\frac{\eta}{k_i} + \frac{1-\eta}{k_r} \right)^{-1}, \tag{50c}$$

representing the arithmetic (50a), geometric (50b), and harmonic (50c) average.

In general, upscaling should be used; see [13] for comparisons of k^A, k^G, k^H. In $d = 1$ upscaled values are the same as harmonically weighted. In this paper, we use harmonic averaging (50c) in our numerical tests and simulations. Based on

Assumption 2.1, we have the uniform bounds

$$k_{min} \le k^H(x,\theta) \le k^G(x,\theta) \le k^A(x,\theta) \le k_{max},\ \forall x \in \Omega, \theta \in \mathbb{R}. \tag{51}$$

A.2. Auxiliary properties of the matrices $\mathscr{M}, \mathscr{B}, \widetilde{\mathscr{K}}$ and $\mathscr{A}$

We now state some useful properties of the matrices $\mathscr{M}, \mathscr{B}, \widetilde{\mathscr{K}}^{-1}$ and $\mathscr{A}$ introduced in Section 3. The matrix $\mathscr{M}$ is a diagonal matrix of the cell-volumes of $\mathscr{T}^h$. We refer the reader to [12] (Section 3.1, Section 7.5) and [44] (Section 3.1, Eq. (15)) for the complete details of $\mathscr{B}$ and $\widetilde{\mathscr{K}}$, and here we only state that $\mathscr{B}$ is a constant matrix with each column having at most two nonzero entries $\in \{-1, 1\}$ and the matrix $\widetilde{\mathscr{K}}$ is a diagonal matrix of the transmissibilities associated with each edge of $\mathscr{T}^h$. For example, the transmissibility $T_{i+\frac{1}{2},j}$ associated with $\gamma_{i+\frac{1}{2},j}$ is defined as

$$T_{i+\frac{1}{2},j} = h_{y,j}\left(\frac{1}{2}h_{x,i}\widetilde{k}_{i,j}^{-1} + \frac{1}{2}h_{x,i+1}\widetilde{k}_{i+1,j}^{-1}\right)^{-1}, \tag{52}$$

so that with $\psi_h = \psi_{i+\frac{1}{2},j}$ in (20b) we get

$$h_{y,j}Q^n_{i+\frac{1}{2},j} = -T_{i+\frac{1}{2},j}(\Theta^n_{i+1,j} - \Theta^n_{i,j}). \tag{53}$$

The right hand side of (53) also explains how the nonzero entries of $\mathscr{B}$ are $\in \{-1, 1\}$.

The matrix $\mathscr{A} = \mathscr{B}\widetilde{K}^{-1}\mathscr{B}^T$ is at least symmetric positive definite (SPD) (and at least positive semidefinite for Neumann boundary conditions). We will now show that $\mathscr{A}$ is weakly diagonal dominant (see Lemma A.1 for the definition). Consider a cell $\omega_{i,j} \in \mathscr{T}^h$. For simplicity of exposition, we let $\omega_{i,j}$ be an interior cell. Then, using the basis functions $\eta_h = \mathbf{1}_{i,j}$ and $\psi_h = \psi_{i\pm\frac{1}{2},j}, \psi_{i,j\pm\frac{1}{2}}$ in (20) gives

$$\begin{aligned} &h_{x,i}h_{y,k}W^n_{i,j} + \tau_n[T_{i+\frac{1}{2},j}(\Theta^n_{i,j} - \Theta^n_{i+1,j}) + T_{i-\frac{1}{2},j}(\Theta^n_{i,j} - \Theta^n_{i-1,j}) + \\ &+T_{i,j+\frac{1}{2}}(\Theta^n_{i,j} - \Theta^n_{i,j+1}) + T_{i,j-\frac{1}{2}}(\Theta^n_{i,j} - \Theta^n_{i,j-1})] = h_{x,i}h_{y,k}W^{n-1}_{i,j} + \tau_n F^n_{i,j}. \end{aligned} \tag{54}$$

Or,

$$\begin{aligned} &h_{x,i}h_{y,k}W^n_{i,j} + \tau_n\left(T_{i-\frac{1}{2},j} + T_{i,j+\frac{1}{2}} + T_{i+\frac{1}{2},j} + T_{i,j-\frac{1}{2}}\right)\Theta^n_{i,j} + \tau_n\left(-T_{i+\frac{1}{2},j}\right)\Theta^n_{i+1,j} + \\ &\tau_n\left(-T_{i-\frac{1}{2},j}\right)\Theta^n_{i-1,j} + \tau_n\left(-T_{i,j+\frac{1}{2}}\right)\Theta^n_{i,j+1} + \tau_n\left(-T_{i,j-\frac{1}{2}}\right)\Theta^n_{i,j-1} = h_{x,i}h_{y,k}W^{n-1}_{i,j} + \tau_n F^n_{i,j}. \end{aligned} \tag{55}$$

Comparing (55) with the (22), we establish that the row of $\mathscr{A}$ corresponding to the degree of freedom $\Theta^n_{i,j}$ has the entries

$$\left\{\left(T_{i-\frac{1}{2},j} + T_{i,j+\frac{1}{2}} + T_{i+\frac{1}{2},j} + T_{i,j-\frac{1}{2}}\right), -T_{i+\frac{1}{2},j}, -T_{i-\frac{1}{2},j}, -T_{i,j+\frac{1}{2}}, -T_{i,j-\frac{1}{2}}\right\}, \tag{56}$$

with the first entry in (56) being the diagonal entry. This proves that $\mathscr{A}$ is row-wise weakly diagonally dominant. Since $\mathscr{A}$ is symmetric, it is also column-wise weakly diagonally dominant.

We will use of the following result on weakly diagonally dominant matrices from [64] (Thm. A.2).

Lemma A.1. *Let $X \in \mathbb{R}^I \times \mathbb{R}^I$ be a column-wise weakly diagonally dominant with non-negative main diagonal and non-positive off-diagonal elements, i.e.,*

$$\begin{aligned} &X_{j,j} \ge \sum_{i=1, i\ne j}^{I} |X_{i,j}|,\ \forall 1 \le j \le I, \\ &X_{j,j} \ge 0,\ \forall 1 \le j \le I,\ X_{i,j} \le 0,\ \forall 1 \le i, j \le I,\ i \ne j. \end{aligned}$$

Then $\|(I+X)^{-1}\|_1 \le 1$.

A.3. Supplemental data

In this section, we provide information for the narrative in Section 6.

A.3.1. Orders of convergence for the linear heat equation

Example A.1. Let $\Omega = (0, 0.2)$ [m] be occupied with water with material properties as in Table 5. We choose the initial condition $w_0 = \alpha^{ST}(\theta_0), \theta_0 = -4$ [°C] and boundary conditions

$$\theta(0,t) = \theta_0,\ \theta(0.2,t) = \theta_0 + \frac{2t}{5000},\ \forall t > 0. \tag{57}$$

The simulations in Example 6.2 are run over $t \in (0, 5000)$ [s]. We consider grid size $h \in \{0.4, 0.2, 0.1\} \times 10^{-2}$ [m] and time step $\tau = (5 \times 10^4)h$ [s] and $\tau = (5 \times 10^7)h^2$ [s]. The results are tabulated in Table 13.

Table 13
Results of Example A.1. Orders of convergence are obtained using fine grid solution computed using $h^{fine} = 2 \times 10^{-3}$ [cm] and $\tau^{fine} = 1$ [s].

Case	τ	$\|\theta_{err}\|_{\infty,2}$	$\|\theta_{err}\|_{\infty,1}$	$\|\theta_{err}\|_{2,2}$	$\|w_{err}\|_{\infty,2}$	$\|w_{err}\|_{\infty,1}$	$\|w_{err}\|_{2,2}$	$\|q_{err}\|_{\infty,2}$	$\|q_{err}\|_{\infty,1}$	$\|q_{err}\|_{2,2}$
Example A.1										
Linear	$O(h)$	0.99	0.99	0.99	0.99	0.99	0.99	0.76	1.00	0.97
heat	$O(h^2)$	1.99	1.99	1.99	1.99	1.99	1.99	1.52	1.99	1.92

Table 14
Results for Example 6.3(i) when Dirichlet boundary conditions are used.

Model	h [cm]	τ [h]	P0-P0-Θ		P0-P0-W	
			Max/min/mean iter.	τ reduced?	Max/min/mean iter.	τ reduced?
Adapted L	5	120	10/1/2.6	No	7/1/2.2	No
		24	5/1/2.4	≈0.18 [h]	5/1/2.0	No
		1	4/1/2.0	≈0.12 [h]	3/1/1.8	No
	1	120	10/1/2.3	No	7/1/2.1	No
		24	6/1/2.3	No	8/1/1.9	No
		1	4/1/2.0	No	3/1/1.7	No
	0.2	120	10/1/2.1	No	6/1/2.2	No
		24	6/1/2.0	No	7/1/1.9	No
		1	4/1/1.8	No	3/1/1.4	No
Adapted W	5	120	7/2/2.7	No	6/1/2.1	No
		24	5/2/2.8	No	4/1/2.0	No
		1	5/2/3.3	No	3/1/2.1	No
	1	120	6/1/2.4	No	7/1/2.0	No
		24	6/1/2.4	No	7/1/1.9	No
		1	5/2/3.0	No	4/1/2.1	No
	0.2	120	6/1/2.2	No	6/1/2.1	No
		24	6/1/2.1	No	7/1/1.9	No
		1	5/2/2.7	No	4/1/2.0	No
Adapted M	5	120	7/1/2.4	No	7/1/2.1	No
		24	5/1/2.0	No	5/1/1.8	No
		1	4/1/1.8	No	3/1/1.5	No
	1	120	7/1/2.1	No	7/1/2.0	No
		24	5/1/1.9	No	7/1/1.7	No
		1	4/1/1.7	No	4/1/1.4	No
	0.2	120	7/1/2.0	No	6/1/2.1	No
		24	6/1/1.8	No	7/1/1.7	No
		1	4/1/1.6	No	4/1/1.3	No

We obtain order 1 and 2 convergence for θ, w and q when using $\tau = O(h)$ and $O(h^2)$, respectively. This is in accordance with the estimates (23).

A.3.2. Robustness of our P0-P0 algorithms in homogeneous permafrost scenarios.

Here we provide the results for Example 6.3. For the case when Dirichlet and Neumann boundary conditions are used, the results are tabulated in Tables 14 and 15, respectively.

A.4. Error norms

We use the following formulas to compute the integrals in the error norms

$$(f,g) = \sum_{j=1}^{N_\omega} f(x_j) g(x_j) h_j, \tag{58a}$$

$$\|f\|_{2,2} = \left(\sum_{n=1}^{N} \tau_n \|f(\cdot,t_n)\|_2^2 \right)^{\frac{1}{2}}, \quad \|f(\cdot,t_n)\|_2 = \left(\sum_{j=1}^{N_\omega} h_j |f(x_j,t_n)|^2 \right)^{\frac{1}{2}}, \tag{58b}$$

$$\|f\|_{\infty,q} = \max_{1\le n\le N} \left[\left(\sum_{j=1}^{N_\omega} h_j |f(x_j,t_n)|^q \right)^{\frac{1}{q}} \right], \quad q \in \{1,2\}, \tag{58c}$$

where $x_j \in \omega_j$ is the center of the cell ω_j and $h_j = |\omega_j|$ is the size of the cell.

Table 15
Results for Example 6.3(ii) when Neumann boundary conditions are used.

Model	h [cm]	τ [h]	P0-P0-Θ		P0-P0-W	
			Max/min/mean iter.	τ reduced?	Max/min/mean iter.	τ reduced?
Adapted L	5	120	5/2/3.3	≈0.4 [h]	4/2/2.8	No
		24	4/1/2.7	≈1.5 [h]	4/1/2.0	No
		1	4/1/1.9	0.5 [h]	2/1/1.9	No
	1	120	5/2/3.5	≈1.8 [h]	6/2/3.2	No
		24	5/1/2.8	No	5/1/2.3	No
		1	4/1/1.9	No	3/1/1.7	No
	0.2	120	7/2/3.6	7.5 [h]	7/2/3.4	No
		24	5/1/2.9	No	5/1/2.5	No
		1	4/1/2.1	No	4/1/1.9	No
Adapted W	5	120	6/1/3.6	60 [h]	4/1/2.7	No
		24	4/1/3.2	12 [h]	3/1/2.2	No
		1	5/1/3.5	No	3/1/1.9	No
	1	120	7/1/3.7	12 [h]	6/1/3.0	No
		24	6/1/3.4	No	5/1/2.6	No
		1	5/1/3.5	No	3/1/2.2	No
	0.2	120	7/1/3.9	No	6/1/3.1	No
		24	6/1/3.5	No	5/1/2.7	No
		1	6/1/3.7	No	4/1/2.7	No
Adapted M	5	120	5/1/3.0	No	4/1/2.5	No
		24	4/1/2.6	3 [h]	4/1/2.0	No
		1	4/1/1.8	No	2/1/1.8	No
	1	120	5/1/3.0	3 [h]	5/1/2.8	No
		24	5/1/2.7	12 [h]	5/1/2.3	No
		1	4/1/1.9	No	3/1/1.9	No
	0.2	120	6/1/3.1	No	6/1/3.0	No
		24	5/1/2.8	12 [h]	6/1/2.4	No
		1	4/1/1.9	No	4/1/1.9	No

References

[1] M. Sandells, D. Flocco, Introduction to the Physics of the Cryosphere, Morgan and Claypool, 2014.
[2] T. Osterkamp, C. Burn, Permafrost, in: J.R. Holton (Ed.), Encyclopedia of Atmospheric Sciences, Academic Press, Oxford, 2003, pp. 1717–1729.
[3] O.B. Andersland, B. Ladanyi, Frozen Ground Engineering, second ed., Wiley; ASCE, Hoboken, NJ, 2004, [Reston, Va.].
[4] P.J. Williams, M.W. Smith, The Frozen Earth: Fundamentals of Geocryology, in: Studies in Polar Research, Cambridge University Press, 1989.
[5] D.J. Nicolsky, V.E. Romanovsky, G.S. Tipenko, D.A. Walker, Modeling biogeophysical interactions in nonsorted circles in the low arctic, J. Geophys. Res.: Biogeosci. 113 (3) (2008).
[6] Y. Zhang, R. Michalowski, Thermal-hydro-mechanical analysis of frost heave and thaw settlement, J. Geotech. Geoenviron. Eng. (2015).
[7] H. Liu, P. Maghoul, A. Shalaby, A. Bahari, Thermo-hydro-mechanical modeling of frost heave using the theory of poroelasticity for frost-susceptible soils in double-barrel culvert sites, Transp. Geotech. 20 (2019) 100251.
[8] H. Zhang, J. Zhang, Z. Zhang, J. Chen, Y. You, A consolidation model for estimating the settlement of warm permafrost, Comput. Geotech. 76 (2016) 43–50.
[9] J. Beddrich, S. Gupta, B. Wohlmuth, G. Chiogna, The importance of topographic gradients in alpine permafrost modeling, Adv. Water Resour. 170 (2022) 104321.
[10] N. Vohra, M. Peszynska, Iteratively coupled mixed finite element solver for thermo-hydro-mechanical modeling of permafrost thaw, 2023, in revision.
[11] M. Peszynska, Z. Hilliard, N. Vohra, Coupled energy and flow models in permafrost from pore- to Darcy scale: modeling and approximation, 2023, submitted.
[12] L. Bigler, M. Peszynska, N. Vohra, Heterogeneous Stefan problem and permafrost models with p0-p0 finite elements and fully implicit monolithic solver, Electron. Res. Arch. 30 (4) (2022) 1477–1531.
[13] M. Peszynska, N. Vohra, L. Bigler, Upscaling an extended heterogeneous stefan problem from the pore-scale to the Darcy scale in permafrost, SIAM Multiscale Model. Simul. (2023) in press.
[14] A. Visintin, Models of Phase Transitions, first ed., Birkhäuser, Boston, MA, 1996.
[15] R.H. Nochetto, C. Verdi, The combined use of a nonlinear chernoff formula with a regularization procedure for two-phase stefan problems, Numer. Funct. Anal. Optim. 9 (11–12) (1988) 1177–1192.
[16] E. Magenes, R.H. Nochetto, C. Verdi, Energy error estimates for a linear scheme to approximate nonlinear parabolic problems, ESAIM: M2AN 21 (4) (1987) 655–678.
[17] C. Verdi, A. Visintin, Error estimates for a semi-explicit numerical scheme for Stefan-type problems, Numer. Math. 52 (2) (1987) 165–186/88.
[18] J. Rulla, N.J. Walkington, Optimal rates of convergence for degenerate parabolic problems in two dimensions, SIAM J. Numer. Anal. (33) (1993) 56–67.
[19] R.E. White, An enthalpty formulation of the stefan problem, SIAM J. Numer. Anal. 19 (1982) 1129–1157.
[20] R.H. Nochetto, M. Paolini, C. Verdi, A fully discrete adaptive nonlinear chernoff formula, SIAM J. Numer. Anal. 30 (4) (1993) 991–1014.
[21] V. Alexiades, A.D. Solomon, Mathematical Modeling of Melting and Freezing Processes, Hemisphere, Washington, 1993.
[22] J.A. Wheeler, Simulation of heat transfer from a warm pipeline buried in permafrost, in: AICHE Paper 27b Presented 74th National Meeting, 1973, pp. 267–284.
[23] D. Nicolsky, V. Romanovsky, G. Tipenko, Using in-situ temperature measurements to estimate saturated soil thermal properties by solving a sequence of optimization problems, Cryosphere 1 (2007).
[24] D. Nicolsky, V. Romanovsky, G. Panteleev, Estimation of soil thermal properties using in-situ temperature measurements in the active layer and permafrost, Cold Reg. Sci. & Technol. 55 (2009) 120–129.

[25] V. Garayshin, D. Nicolzsky, V. Romanovsky, Numerical modeling of two-dimensional temperature field dynamics across non-deforming ice-wedge polygons, Cold Reg. Sci. & Technol. 161 (2019) 115–128.
[26] D. Sergueev, G. Tipenko, V. Romanovsky, Mountain permafrost thickness evolution under influence of long-term climate fluctuations (results of numerical simulation), in: Proceedings of the VII International Permafrost Conference, Switzerland, 2003, pp. 1017–1021.
[27] S. Marchenko, V. Romanovsky, G. Tipenko, Numerical modeling of spatial permafrost dynamics in alaska, in: Proceedings of Ninth International Conference on Permafrost, Ninth International Conference on Permafrost, 2008, pp. 1125–1130.
[28] F. Ling, T. Zhang, A numerical model for surface energy balance and thermal regime of the active layer and permafrost containing unfrozen water, Cold Reg. Sci. & Technol. 38 (1) (2004) 1–15.
[29] E.E. Jafarov, S.S. Marchenko, V.E. Romanovsky, Numerical modeling of permafrost dynamics in alaska using a high spatial resolution dataset, Cryosphere 6 (3) (2012) 613–624.
[30] M.T. Jorgenson, Y.L. Shur, E.R. Pullman, Abrupt increase in permafrost degradation in arctic alaska, Geophys. Res. Lett. 33 (2) (2006).
[31] M. Kanevskiy, Y. Shur, T. Jorgenson, D.R. Brown, N. Moskalenko, J. Brown, D.A. Walker, M.K. Raynolds, M. Buchhorn, Degradation and stabilization of ice wedges: Implications for assessing risk of thermokarst in northern alaska, Geomorphology 297 (2017) 20–42.
[32] J.C. Rogers, A.E. Berger, M. Ciment, The alternating phase truncation method for numerical solution of a stefan problem, SIAM J. Numer. Anal. 16 (4) (1979) 563–587.
[33] J.M. McKenzie, C.I. Voss, D.I. Siegel, Groundwater flow with energy transport and water–ice phase change: Numerical simulations, benchmarks, and application to freezing in peat bogs, Adv. Water Resour. 30 (4) (2007) 966–983.
[34] J.G. Dash, A.W. Rempel, J.S. Wettlaufer, The physics of premelted ice and its geophysical consequences, Rev. Modern Phys. 78 (2006) 695–741.
[35] C.W. Lovell, Temperature effects on phase composition and strength of partially-frozen soil, Highw. Res. Board Bull. (1957).
[36] D.M. Anderson, A.R. Tice, Predicting unfrozen water contents in frozen soils from surface area measurements, Highw. Res. Rec. (1972).
[37] R.L. Michalowski, A constitutive model of saturated soils for frost heave simulations, Cold Reg. Sci. & Technol. 22 (1) (1993) 47–63.
[38] T.E. Osterkamp, Freezing and thawing of soils and permafrost containing unfrozen water or brine, Water Resour. Res. 23 (12) (1987) 2279–2285.
[39] V. Romanovsky, T. Osterkamp, Effects of unfrozen water on heat and mass transport in the active layer and permafrost, Permafr. Periglac. Process. 11 (2000) 219–239.
[40] M. Ulbrich, Semismooth Newton Methods for Variational Inequalities and Constrained Optimization Problems in Function Spaces, in: MOS-SIAM Series on Optimization, vol. 11, Society for Industrial and Applied Mathematics (SIAM), Philadelphia, PA, 2011.
[41] R.E. Showalter, Mathematical formulation of the Stefan problem, Internat. J. Engrg. Sci. 20 (8) (1982) 909–912.
[42] S. Gupta, The Classical Stefan Problem: Basic Concepts, Modelling and Analysis, first ed., Elsevier Science, 2003.
[43] T.F. Russell, M.F. Wheeler, 2. Finite element and finite difference methods for continuous flows in porous media, 1983, pp. 35–106.
[44] M. Peszynska, E. Jenkins, M.F. Wheeler, Boundary conditions for fully implicit two-phase flow model, in: X. Feng, T.P. Schulze (Eds.), Recent Advances in Numerical Methods for Partial Differential Equations and Applications, in: Contemporary Mathematics Series, vol. 306, American Mathematical Society, 2002, pp. 85–106.
[45] A. Weiser, M.F. Wheeler, On convergence of block-centered finite differences for elliptic problems, SIAM J. Numer. Anal. 25 (2) (1988) 351–375.
[46] T. Arbogast, M.F. Wheeler, N.-Y. Zhang, A nonlinear mixed finite element method for a degenerate parabolic equation arising in flow in porous media, SIAM J. Numer. Anal. 33 (4) (1996) 1669–1687.
[47] E. Schneid, P. Knabner, F. Radu, A priori error estimates for a mixed finite element discretization of the Richards' equation, Numer. Math. 98 (2) (2004) 353–370.
[48] C.S. Woodward, C.N. Dawson, Analysis of expanded mixed finite element methods for a nonlinear parabolic equation modeling flow into variably saturated porous media, SIAM J. Numer. Anal. 37 (3) (2000) 701–724, (electronic).
[49] S. Del Giudice, G. Comini, R.W. Lewis, Finite element simulation of freezing processes in soils, Int. J. Numer. Anal. Methods Geomech. 2 (3) (1978) 223–235.
[50] K. Hansson, J. Simunek, Jiri, M. Mizoguchi, L.-C. Lundin, M. Van Genuchten, Water flow and heat transport in frozen soil, Vadose Zone J. - VADOSE ZONE J 3 (2004) 527–533.
[51] Q.T. Pham, Comparison of general-purpose finite-element methods for the stefan problem, Numer. Heat Transfer B 27 (4) (1995) 417–435.
[52] V. Voller, C.R. Swaminathan, B.G. Thomas, Fixed grid techniques for phase change problems: A review, Internat. J. Numer. Methods Engrg. 30 (1990) 875–898.
[53] C. Bonacina, G. Comini, A. Fasano, M. Primicerio, Numerical solution of phase change problems, Int. J. Heat Mass Transfer 16 (1973) 1825–1832.
[54] G. Comini, S. Guidice, R. Lewis, O. Zienkiewicz, Finite element solution of non-linear heat conduction problems with special reference to phase change, Internat. J. Numer. Methods Engrg. 8 (1974) 613–624.
[55] K. Morgan, R.W. Lewis, O.C. Zienkiewicz, An improved algrorithm for heat conduction problems with phase change, Internat. J. Numer. Methods Engrg. 12 (7) (1978) 1191–1195.
[56] C.T. Kelley, Iterative Methods for Linear and Nonlinear Equations, Society for Industrial and Applied Mathematics, 1995.
[57] L. Qi, J. Sun, A nonsmooth version of Newton's method, Math. Program. 58 (1) (1993) 353–367.
[58] I. Pop, F. Radu, P. Knabner, Mixed finite elements for the Richards' equation : linearization procedure, J. Comput. Appl. Math. 168 (1–2) (2004) 365–373.
[59] C. Evans, S. Pollock, L.G. Rebholz, M. Xiao, A proof that anderson acceleration improves the convergence rate in linearly converging fixed-point methods (but not in those converging quadratically), SIAM J. Numer. Anal. 58 (1) (2020) 788–810.
[60] W.H. Press, S.A. Teukolsky, W.T. Vetterling, B.P. Flannery, Numerical Recipes 3rd Edition: The Art of Scientific Computing, third ed., Cambridge University Press, USA, 2007.
[61] Permafrost Laboratory, Geopphysical Institute, university of alaska fairbanks. https://permafrost.gi.alaska.edu. Retrieved in 2023.
[62] J. Brown, K.M. Hinkel, F.E. Nelson, The circumpolar active layer monitoring (calm) program: Research designs and initial results, Polar Geogr. 24 (3) (2000) 166–258.
[63] Climate-active layer-permafrost system. https://www2.gwu.edu/calm/. Retrieved in 2023.
[64] J. Fuhrmann, Existence and uniqueness of solutions of certain systems of algebraic equations with off-diagonal nonlinearity, Appl. Numer. Math. 37 (3) (2001) 359–370.